ANNUAL REVIEW OF HEAT TRANSFER

Volume 6

Edited by

Chang-Lin Tien

Chancellor and A. Martin Berlin Professor
University of California, Berkeley, California

begell house, inc.
new york, wallingford (u.k.)

CHAPTER

FOUR

LIQUID JET IMPINGEMENT

John H. Lienhard V

ABSTRACT

Liquid jet impingement is appealing because the liquid supply arrangement is relatively simple and low thermal resistances can be routinely achieved. When operated at high velocity, jets can remove fluxes several times that at the surface of the sun. This article reviews heat transfer and flow phenomena during unsubmerged liquid jet impingement and provides correlations for calculating the heat transfer coefficients. Convective transport without phase change is covered in detail. Results for the stagnation zone are given first, followed by those for the regions downstream. Both axisymmetric and planar jets are considered. The splattering that accompanies turbulent jet impingement is described, and other aspects of liquid jet impingement cooling are surveyed briefly.

NOMENCLATURE

Roman Letters

A_{2n} constants in Eq. 7.

B dimensionless velocity gradient, $2\frac{d}{u_f}\frac{du_e}{dr}$ or $2\frac{w}{u_f}\frac{du_e}{dx}$.

C dimensional stagnation-point velocity gradient, du_e/dr or du_e/dx.

C_c contraction coefficient for liquid jets, jet area/nozzle area.

C_f skin friction coefficient.

c_p liquid specific heat capacity at constant pressure (J/kgK).

1-56700-026-6/95/$0.00 + $0.50

d jet diameter, fully contracted (m).
d_o orifice diameter (m).
d_t jet diameter at target (m).
D diameter of cooled target (m).
$f(\eta)$ velocity similarity function.
$\mathrm{Fr_d}$ jet Froude number, $u_f/\sqrt{gd}$.
$\mathrm{Fr_h}$ supercritical film Froude number, $u_h/\sqrt{gh}$.
g gravitational body force, 9.81 m/s^2.
$g(\eta)$ temperature similarity function.
$g'(0)$ heat transfer function of Prandtl number, Eq. 34 or 33.
h local heat transfer coefficient, $q_w/(T_w - T_f)$, (W/m^{2}K).
$h(r)$ thickness of axisymmetric liquid sheet (m).
k thermal conductivity of liquid (W/m K), or rms surface roughness (m).
k^* dimensionless surface roughness, k/d.
k_w thermal conductivity of target.
l distance between nozzle and target plate (m).
l_o distance between nozzle and target plate for onset of splattering (m).
$\mathrm{Nu_d}$ local Nusselt number based on jet diameter, $q_w d/k(T_w - T_f)$.
$\mathrm{Nu_x}$ local Nusselt number downstream for planar jet, $q_w x/k(T_w - T_f)$.
p local pressure in liquid (Pa).
p_∞ ambient pressure (Pa).
p_{stgn} stagnation pressure (Pa).
$p_e(r)$ pressure distribution along the wall (Pa).
P_o gauge pressure in plenum, same as stagnation pressure (Pa).
$\mathrm{P_{2n}}$ Legendre function of 2n order.
Pr Prandtl number of liquid.
Q volume flow rate of jet (m^3/s).
Q_s volume flow rate of splattered liquid (m^3/s).
q_w wall heat flux (W/m^2).
r radius coordinate in spherical coordinates, or radius coordinate in cylindrical coordinates (m).
r_h radius at which turbulence is fully developed (m).
r_j radius of hydraulic jump (m).
r_o radius at which viscous boundary layer reaches free surface (m).
r_s radius at which subcritical liquid has depth s (m).
r_t radius at which turbulent transition begins (m).
r_1 radius at which thermal boundary layer reaches free surface (m).
$\mathrm{Re_d}$ Reynolds number of circular jet, $u_f d/\nu$.

$\mathrm{Re_w}$ Reynolds number of planar jet, $u_f w/\nu$.
$\mathrm{Re_x}$ local Reynolds number of planar jet, $u_e(x)x/\nu$.
$\mathrm{Re_{xc}}$ transition Reynolds number of planar jet.
s depth of subcritical liquid sheet (m).
St Stanton number, $q_w/[\rho c_p u_m(T_w - T_{sf})]$.
t wall thickness (m).
T liquid temperature (K).
T_f temperature of incoming liquid jet (K).
T_w temperature of wall (K).
T_{sf} liquid surface temperature (K).
Tu freestream turbulence intensity, u_{rms}/u_f.
u,v liquid velocity components in radial, axial direction of cylindrical coordinates or in x,y direction of Cartesian coordinates (m/s).
u' rms turbulent velocity fluctuation in jet (m/s).
u_f bulk velocity of incoming jet (m/s).
u_h velocity of liquid sheet averaged across thickness h (m/s).
u_m free surface velocity of liquid sheet (m/s).
u_t bulk velocity of gravity affected jet at target (m/s).
$u_e(r)$ radial velocity just outside boundary layer (m/s).
$u_e(x)$ planar velocity just outside boundary layer (m/s).
V_{max} centerline velocity of incoming jet (m/s).
w width of planar impinging jet (m).
We jump Weber number, $s\sqrt{\rho g/\sigma}$.
$\mathrm{We_d}$ jet Weber number, $\rho u_f^2 d/\sigma$.
x coordinate along the wall in planar flow or coordinate along jet axis for roughness data (m).
y axial coordinate in cylindrical coordinates or vertical coordinate in Cartesian coordinates (m).

Greek Letters

α thermal diffusivity of liquid (m^2/s).
β coefficient in similarity equation.
δ 99% thickness of momentum boundary layer (m).
δ_{rms} local rms surface roughness of turbulent jet (m).
δ_t conduction thickness of thermal boundary layer, or integral solution for thermal boundary layer thickness (m).
η similarity coordinate or dimensionless wavenumber.
θ polar angle of spherical coordinates.

μ dynamic viscosity of liquid (kg/m s).
ν kinematic viscosity of liquid (m^2/s).
ξ splattered fraction of impinging jet's liquid, Q_s/Q.
ρ density of liquid (kg/m^3).
σ liquid-gas surface tension (N/m).
ϕ velocity potential (m^2/s).
ψ stream function (m^2/s).
ω scaling parameter for splattering, Eq. 84.

Superscripts

$\overline{(\,)}$ average value

1 INTRODUCTION

Liquid jet impingement cooling offers very low thermal resistances and is relatively simple to implement. Liquid jets are easily created using a straight tube or a contracting nozzle, and this nozzle can be aimed directly toward the region of a heat load. When the jet strikes the target surface, it forms a very thin stagnation-zone boundary layer that offers little resistance to heat flow. Convective heat transfer coefficients can routinely reach 10 to 100 kW/m^2K.

These high heat transfer coefficients make liquid jet impingement attractive in situations where a high heat load must be removed while maintaining a minimum temperature or temperature difference within the system. For example, in some semiconductor laser systems, junction temperatures must be held below 150°C, while heat loads may reach 10 MW/m^2. Much attention has been given to jet impingement cooling of electronics.

An impinging jet defines its own flow field, often without the need for added channeling or target modifications. Jets are particularly useful when cooling systems must not add interfering hardware or make structural changes to the cooled object. For example, a fixed nozzle at the end of a processing line can cool each successive item passed under it, and in some automotive engines, oil jets cool the undersides of the piston crowns.

Liquid jets can also carry extremely high heat fluxes, if the velocities are such as to produce a high stagnation pressure. Small diameter water jets at speeds near 100 m/s have removed heat loads of up to 400 MW/m^2. Liquid jets are well-suited for cooling very localized, high-flux heat sources.

The jets of interest in the present article are unsubmerged jets, those that travel through a gas between the nozzle and the target (Figure 1). These jets are only similar to submerged jets in the stagnation region, and then only when the submerged jet is less than about 5 diameters in length.

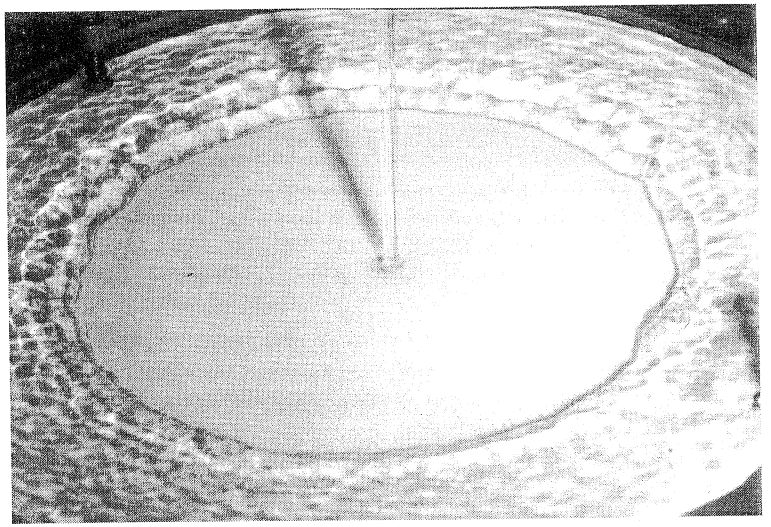

Figure 1 Laminar impinging jet: $Re_d = 51{,}000$, $d = 5.0$ mm, sharp-edged orifice, adiabatic target.

This review focuses on convective heat transfer for both axisymmetric and planar impinging jets. The effect of nozzle design, which can have a substantial influence on heat transfer, is discussed in Section 2. Theoretical results for the stagnation zone are described in Section 3; the inviscid stagnation flows of jets are a key issue there, as they are necessary in using the more standard boundary layer results. Expressions for calculating the stagnation-zone Nusselt number are given in Section 4.

Downstream of the stagnation zone the boundary layer grows, and convective heat transfer is generally less efficient. Downstream results for laminar jets and for turbulent planar jets are given in Section 5. Turbulent axisymmetric jets are treated separately in Section 6. One specific feature of the latter jets is their tendency to splatter upon impact, sometimes atomizing more than 50% of the jet's liquid. Splattering phenomena are covered in Section 6.1.

Section 7 briefly reviews some additional aspects of jet impingement, specifically: average Nusselt numbers, moving walls, electronics cooling, and boiling. Finally, Section 7.5 describes how liquid jets have sustained the highest steady-state heat fluxes ever reported.

2 NOZZLES FOR LIQUID JETS

The nozzle that produces a jet determines its velocity profile and turbulence characteristics, as well as its contraction coefficient and its propensity for splattering or breakup. Each of these features can have a significant impact on the heat transfer characteristics of the jet, particularly in the stagnation zone.

A relatively large literature addresses the design of nozzles for liquid jets. Most of this literature is directed toward application to fire-fighting nozzles and jet-cutting nozzles, where the general design objectives are to achieve a high discharge coefficient and to inhibit jet breakup and spreading [1-5]. Those aims are generally best met by minimizing turbulence in the liquid leaving the nozzle.

In the context of cooling nozzles, the stability of the jet is important mainly for large nozzle-to-target separations, where breakup of the jet may disperse the coolant and splattering of the jet can reduce the flow along the wall. When the nozzle-to-target separation is small (a few nozzle diameters or less), breakup and splattering are less of an issue. Instead, velocity-profile nonuniformity and turbulence are of greater significance, because they can markedly increase the stagnation-zone heat transfer. These effects are illustrated in Figure 8, below.

The velocity profile and turbulence level must usually be determined for each individual nozzle configuration. Key features of a nozzle that affect these properties are [4]: (1) the contraction ratio, D/d, from the upstream diameter, D, to the outlet diameter, d_o, of the nozzle; (2) the boundary layer development within the nozzle, generally a function of the length of the contracted portion of the nozzle and of the interior roughness of the nozzle; and (3) the interior streamlining or contraction angle of the nozzle. Some typical axisymmetric nozzles are shown in Figure 2.

A strong contraction will tend to damp turbulence in the jet. Sharp-edged orifices (Figure 2a), in particular, can produce laminar jets having uniform velocity profiles, provided that the orifice diameter, d_o, is small relative to the size of the plenum above it. Such jets experience an additional contraction after leaving the nozzle, so that the ratio of jet cross-sectional area to orifice area is less than unity; this ratio is called the contraction coefficient and for sharp-edged nozzles its value is $C_c = 0.6$ [6,7]*. However, the high contraction ratio and stable upstream flow needed to produce uniform laminar jets are not usually achieved in practice. For example, nozzle contraction ratios are limited by the jet diameter (d) required and a maximum feasible supply line size (D), and turbulence or secondary flows upstream of the nozzle are seldom fully damped.

Boundary layer development along the walls of the nozzle is a primary cause of velocity nonuniformity in the jet for both laminar and turbulent flow. The extent of boundary layer growth depends on both the length of the nozzle and the degree of contraction (or flow acceleration) within the nozzle. The long straight tube nozzles (Figure 2d) used in many impingement cooling experiments have no contraction and may allow complete boundary layer development. Their flow is fully developed if the nozzle length, L, is more than about 40 diameters, with laminar flow occurring for Reynolds numbers below 2000 to 4000. The laminar jets obtain a parabolic velocity profile, and fully developed turbulent jets take on a blunter nonuniform profile.

A strong contraction suppresses boundary layer growth and turbulent transition in the boundary layer, but a terminating straight section beyond the contraction can promote boundary layer development (Figure 2b). In the context of long-throw

*The velocity coefficient is essentially unity.

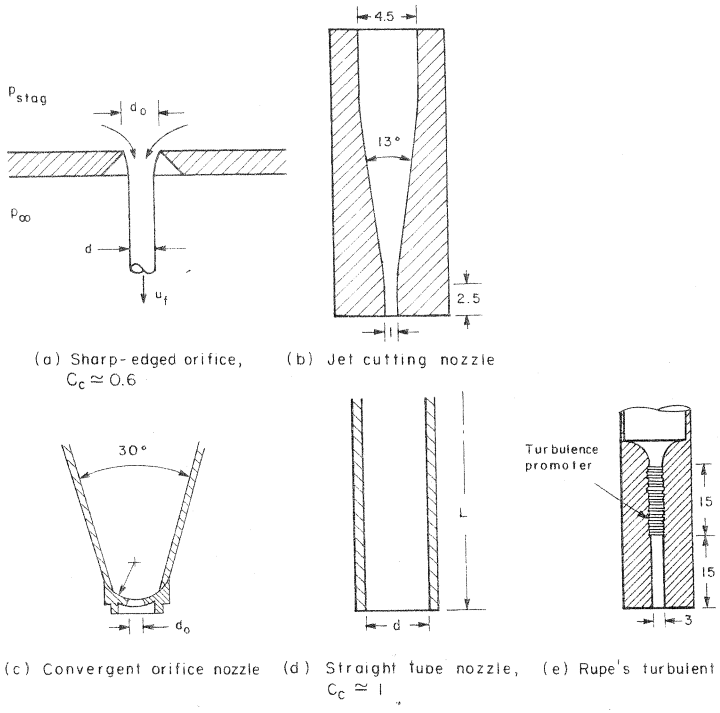

Figure 2 Typical axisymmetric nozzles for liquid jets (dimensions in mm) [3,4,5,7].

nozzles for jets, Hoyt and Taylor [5] developed a contracting nozzle that suppresses boundary layer development (Figure 2c); a similar design was proposed by Rouse et al. [1]. On the other hand, when turbulence is desired for quick jet breakup — or possibly for cooling enhancement — internal roughening of a short nozzle can promote the rapid establishment of turbulence; this technique has been demonstrated by Rupe (Figure 2e) [4].

Interior streamlining of a nozzle's contraction will prevent flow separation, thus reducing head loss and turbulence. For high Reynolds numbers, such streamlining is subject to the same considerations as apply to wind-tunnel contraction design [8]; and nozzles having sophisticated streamlining have been used in several studies [1,2,5]. A more easily machined form, on the other hand, is a converging cone of a small angle; such nozzles have shown good results in several studies (Figure 2bc). Undesired secondary flows or turbulence can be further reduced by adding flow straighteners upstream of the contraction.

In general, the performance of any nozzle will vary with its Reynolds number, owing to changes in boundary layer development, changes the position of laminar/turbulent transition, and at high Re_d, air drag on the jet. For slow small diameter jets,

surface-tension effects can have some influence [7,9]: when $We_d < 100$, the jet contraction is increased, and for We_d below 8, the nozzle chugs rather than flowing steadily. In addition, small irregularities on the lip of a nozzle can cause nonuniformities in the liquid jet surface that promote unsteadiness and breakup.

2.1 Nozzle-to-Target Separation Effects

The distance, l, between a nozzle and the target on which the jet impinges can influence the liquid flow in several ways. First, if the jet is far from the target, turbulence in the jet and air drag on the jet can promote atomization of the liquid. Air drag is likely to be important for Reynolds numbers above 50,000, but its overall impact also depends on the length of the jet [10]. Because jet breakup is treated in great detail in the literature, it is not reviewed here.

Second, turbulence within a long jet causes surface roughness that can lead to splattering of liquid droplets off of the target after the jet impacts. Splattering phenomena are covered in detail in Section 6.1 below. Splattering is of greatest importance at Weber numbers above several thousand and for nozzle-to-target separations of more than about 15 jet diameters.

Third, a large nozzle-to-target separation allows time for viscosity or turbulence to eliminate velocity nonuniformity in the jet, so that the profile tends to become uniform at the jet's bulk velocity. While a number of studies have examined the rate of velocity profile relaxation [11–13], no general criteria appear to have been delineated. However, the experimental results show that: (1) laminar jets may require up to 20 nozzle diameters to relax fully; (2) turbulent jets relax much faster than laminar jets, reaching a nearly uniform profile within 3 to 5 diameters; and (3) the rate of relaxation is not simply a function of Reynolds number, although it clearly depends on jet speed and size.

Fourth, for slow jets flowing vertically downward, gravitational acceleration increases the jet speed and decreases the diameter. The Bernoulli equation and mass convervation show that the jet velocity and diameter at the target, u_t and d_t, are related to the nozzle outlet values by:

$$u_t = \sqrt{u_f^2 + 2gl} \tag{1}$$

$$d_t = d\sqrt{\frac{u_j}{u_t}} \tag{2}$$

From these equations, it follows that the speed at the target is within 10% of u_f (and d_t within 5% of d) if $gl/u_f < 0.1$.

Finally, it should be mentioned that turbulence levels within the liquid may vary with distance from the target, owing to both the growth of liquid surface roughness and the damping effect of viscosity. However, experiments have shown that nozzle-to-target spacing has little net influence on turbulent jet stagnation-zone heat transfer (see Section 4.4.4).

2.2 Submerged Jets and Arrays of Jets

Submerged jets, confined jets, and arrays of jets behave differently than the single, unsubmerged jets that are the focus of this article. However, each of the former types of jet may exhibit stagnation zone behavior similar to the latter type under some conditions.

Several comprehensive reviews have dealt with submerged impinging jets [14,15]. For present purposes, it is useful to note that the stagnation zone of a submerged jet is identical to that of an unsubmerged jet if the submerged jet is within 5 to 6 diameters of the target, so that its core has not begun to mix with surrounding fluid. Downstream of the stagnation zone, however, a submerged nozzle produces a growing turbulent wall jet that behaves quite differently than the liquid sheet produced by an unsubmerged nozzle.

Sometimes an impinging jet may be closely confined. One such design uses a pair of concentric tubes to produce an impinging jet from the inner tube that is confined at larger radius by the slightly longer outer tube. After striking the cooled target, which caps the outer tube, the liquid is drained through the annular region between the outer and inner tubes. This configuration is intended to produce stagnation-zone conditions (and high heat transfer coefficients) along the capping target. Such designs have been used occasionally to cool plasma-arc targets, and results for an electronics-cooling application have been given by Besserman et al. [16].

Arrays of impinging unsubmerged jets have been examined in only a few studies [17,18], although such arrays are common in submerged gas-jet designs. The appeal of a jet array is that more of the target surface can be exposed to the high heat transfer coefficient of the jets' stagnation zones. For unsubmerged jets, the principal drawback of jet arrays is the potentially poor drainage of liquid from the region between adjacent jets, which can cause poor heat transfer there. Nonetheless, development of liquid jet arrays is ongoing, and the possibility of a successful design should not be excluded.

3 STAGNATION ZONE THEORY

This section provides the theoretical description of the stagnation zone flow and heat transfer. The main results are theoretical expressions for the stagnation zone Nusselt number. Experimental support for the theory is cited where it is available.

Near the point of impact, an impinging jet's fluid flow and heat transfer characteristics are described in general terms by the usual results for the stagnation zone. The flow field can be divided into an outer region of essentially inviscid flow and an inner viscous boundary layer region [19]. The two regions are coupled in the usual asymptotic sense by matching the inviscid solution at the wall to the boundary layer

solution at infinity, so that the near-wall inviscid flow defines the freestream of the boundary layer.

The analytical solution of the stagnation-zone boundary layer is a classical problem [20-22], whose results depend primarily on the radial velocity gradient of the inviscid flow near the stagnation point. To adapt stagnation zone boundary layer results to impinging jets, this gradient must be determined. Thus, analysis of the stagnation zone requires first a solution for the inviscid flow of the jet and then application of the boundary solutions for the flow and temperature fields. Together, these lead to expressions for the wall heat flux and the Nusselt number.

3.1 Inviscid Outer Flow

The inviscid flow field of an impinging jet is defined by: a free streamline boundary condition at the liquid surface; an impermeable wall onto which the jet impacts; and assumed forms of the inlet and outlet velocity profiles (Figure 3). If the inlet profile is irrotational (e.g., uniform), the velocity field can be obtained using potential flow theory ($\nabla^2\phi = 0$); otherwise, the Euler equations must be solved.

In all cases, the stagnation-zone flow has radial velocity distribution at the wall given by

$$u_e(r) = Cr + \ldots, \quad r \to 0 \tag{3}$$

for $C = (du_e/dr|_{r=0})$ a constant radial velocity gradient. This result is necessitated by the kinematics of any stagnation zone (for irrotational flow, see Reference 23); the constant C, however, depends on the specific inviscid flow considered. For later use in heat transfer analyses, it is convenient to nondimensionalize the wall gradient:

$$B \equiv 2\frac{d}{u_f}\frac{du_e}{dr}\bigg|_{r=0} \tag{4}$$

The inviscid flow near the stagnation point has a wall pressure distribution given by

$$p_e(r) = p_\infty + \frac{\rho}{2}\left(u_f^2 - u_e(r)^2\right) \tag{5}$$

$$= p_{stgn} - \frac{\rho}{2}u_e(r)^2 \tag{6}$$

for p_∞ the ambient pressure and p_{stgn} the stagnation pressure. If the jet is nonuniform, u_f refers to the centerline velocity of the jet away from the target; if surface tension pressure is significant, only Eq. 6 applies [9]. Measurements of the wall pressure distribution have often been used to determine $u_e(r)$.

The potential flow is independent of Reynolds number and scales with the inlet speed and jet diameter. Low levels of turbulence in the incoming jet are likely to have only slight effects on the mean velocity distribution outside the wall boundary layer, so the inviscid solutions should apply to either laminar or turbulent jets, if those jets have the specified inlet velocity profiles. In addition, the boundary conditions on the free streamline (no shear stress, pressure constant at p_∞) will apply for steady jets of any density; thus, solutions that have been obtained in the context of nonmixing gas jets (no entrainment of surrounding fluid) apply equally well to unsubmerged liquid jets. The similarity between submerged jets and free liquid jets obviously fails once the submerged jet begins to mix with the surrounding fluid.

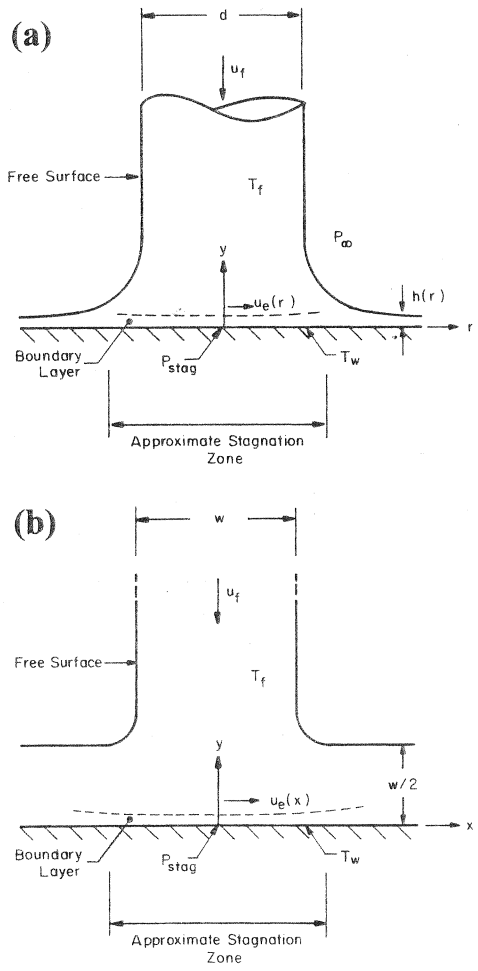

Figure 3 Impinging jet configurations for inviscid flow solutions: (a) axisymmetric; (b) planar.

3.1.1 Uniform Velocity-Profile Circular Jets. Jets of uniform profile are typical of those created by a sharp-edged orifice several diameters downstream of the outlet and at any Reynolds number well above unity. Analysis and experiments on impingement of such jets date from the late 1920s [6]. Schach [24,25] obtained approximate solutions for the velocity and experimental measurements of wall pressure; the solutions and pressure data agreed reasonably well in the sense of Eq. 5. Subsequent analytical solutions for normal impingement were found by Shen [26] and by Strand [27].

More recently, the problem has been revisited in detail by Liu, Gabour, and Lienhard [9], who expanded the velocity potential, ϕ, in a series of Legendre polynomials and obtained numerical solutions for the coefficients, incorporating the liquid surface tension. Their result was

$$\frac{\phi(r,\theta)}{(2u_f d)} = \sum_{n=0}^{\infty} A_{2n}\left(\frac{r}{2d}\right)^{2n} P_{2n}(\cos\theta) \tag{7}$$

for spherical coordinates (r, θ) with origin at the stagnation point and polar axis along the axis of the jet. Values of the coefficients are given in Table 1. The velocity along the wall just outside the boundary layer, $u_e(r) = \partial\phi/\partial r|_{\theta=\pi/2}$, is then

$$\frac{u_e(r)}{u_f} = \sum_{n=1}^{\infty} 2nA_{2n}\left(\frac{r}{2d}\right)^{2n-1} P_{2n}(0) = (-A_2)\left(\frac{r}{2d}\right) + \left(\frac{3A_4}{2}\right)\left(\frac{r}{2d}\right)^3 + \ldots \tag{8}$$

From this, the dimensionless stagnation-point velocity gradient is

$$B = -A_2 = 1.831 \tag{9}$$

for infinite Weber number; lower Weber number values are shown in Figure 4. Values of B from the various investigations are compared in Table 2.

Table 1 Coefficients of Velocity Potential from Liu et al. [9]

We_d	∞	50	25	16.7
A_2	−1.83128	−1.88145	−1.94351	−2.0145
A_4	2.36521	2.85814	3.46923	4.21339
A_6	0.590615	−0.0155255	−0.800645	−1.82463
A_8	−14.8129	−19.0321	−24.3046	−30.7791
A_{10}	13.3533	20.4228	29.3757	40.6072
A_{12}	50.7441	68.7357	91.3149	119.258

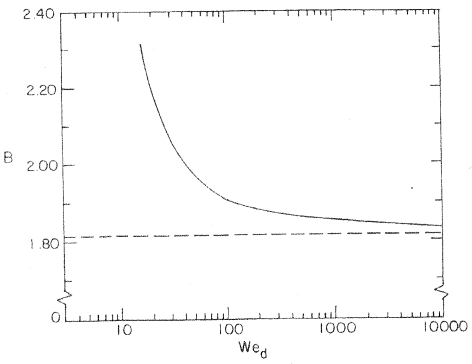

Figure 4 Inviscid stagnation-point velocity gradient, $B = 2(d/u_f)\,(du_e/dr)$, including effect of Weber number for uniform velocity profile [9].

The velocity and pressure distributions along the wall are shown in Figure 5, and Figure 6 shows the calculated pressure field.* Figure 7 shows the vertical distributions of velocity and radial velocity gradient.

The velocity distribution is well approximated by a linear distribution

$$\frac{u}{u_f} = \frac{B}{2}\frac{r}{d} = 0.916\frac{r}{d}, \quad r/d < 0.5 \tag{10}$$

for $r/d < 0.5$, and the pressure distribution can be estimated using this result and Eq. 5 to within about 10% for $r/d < 0.5$. Heat transfer data suggest that the stagnation zone can reasonably be approximated to extend as far as $r/d \approx 0.7$ from the actual stagnation point. For $r/d > 0.7$, boundary layer growth must be taken into account (see Section 5).

3.1.2 Parabolic Velocity-Profile Circular Jets. Jets of parabolic profile are created by a laminar flow issuing from a long circular tube at Reynolds numbers below 2000 to 4000. The parabolic profile will diffuse toward a uniform velocity profile as

Table 2 Velocity Gradients at the Stagnation Point during Laminar Circular Jet Impingement: $B/2 = (d/u_f)\,(du_e/dr)$

Investigators	$B/2$	Jet type	Inlet velocity profile	l/d	We_d
Schach [25]	≈ 0.88	Circular	Uniform	1.5	∞
Shen [26]	0.743	Circular	Uniform	1.5	∞
Strand [27]	0.903	Circular	Uniform	1.0	∞
Liu, Gabour, and	0.916	Circular	Uniform	1.0	∞
Lienhard [9]	0.981	Circular	Uniform	1.0	50
	1.06	Circular	Uniform	1.0	25
	1.16	Circular	Uniform	1.0	16.7
Scholtz andTrass [28]	4.69	Circular	Parabolic	0.05–0.5	∞

*Figure 6 corrects mislabeling of the level curves shown in Liu et al. [9]; Table 2 also incorporates a few corrections.

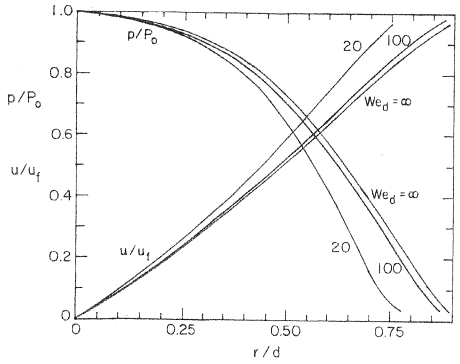

Figure 5 Velocity and pressure variation along the target plate ($y/d = 0$) for several values of Weber number, inviscid flow, and uniform velocity profile [9].

the jet travels to the target, if the jet is long enough for viscosity to act; if the nozzle is within a few diameters of the target, the parabolic distribution should persist.

Inviscid analytical solutions for this case were obtained by Scholtz and Trass [28] for nozzle-to-target spacings of $0.05 < l/d < 0.5$. To leading order, the velocity along the wall near the stagnation point for $l/d = 0.5$ is

$$u_e = 2.323\left(\frac{V_{max}}{d}\right)r, \quad r/d < 0.4 \tag{11}$$

for V_{max} the maximum (centerline) velocity in the nozzle and d the nozzle diameter. To the accuracy of the numerical solutions, the constant in Eq. 11 is unaffected by l/d in the range $0.05 < l/d < 0.5$. Scholtz and Trass also obtained experimental results for velocity and pressure distributions over the range $0.05 < l/d < 6.0$. The experimental results show little sensitivity to l/d for $l/d > 1$. As the nozzle is moved closer than 1 diameter from the target, constriction alters the flow field downstream of the stagnation point; however, at the stagnation point itself, the velocity gradient remains unaffected. The experiments showed that the stagnation-point pressure distribution

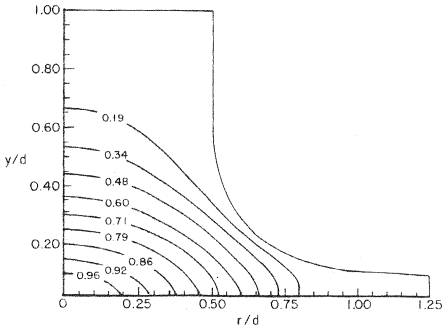

Figure 6 The inviscid pressure distribution, p/P_0, for $We_d \to \infty$ and a uniform velocity profile [9].

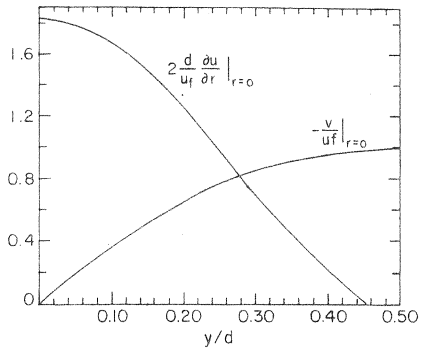

Figure 7 Vertical profiles of downward velocity, v, and radial velocity gradient along jet centerline for uniform profile, inviscid flow as $We_d \to \infty$ [9].

was within 10% of that given by Eqs. 5 and 11 for $r/d < 0.4$ and all nozzle spacings. Note that this is a slightly smaller stagnation zone than is obtained with a uniform jet.

In terms of bulk velocity, $u_f = V_{max}/2$, the dimensionless velocity gradient of the parabolic jet is

$$B = 2\frac{d}{u_f}\frac{du_e}{dr}\bigg|_{r=0} = 4.646 \tag{12}$$

The experimental results generally support this equation for $0.05 < l/d < 6$. Most importantly, the parabolic-profile jet has a velocity gradient 2.5 times higher than the uniform jet, which (as we shall see below) raises the heat transfer coefficent substantially.

3.1.3 Results for Planar Jets. The planar impinging jet with uniform velocity profile can be solved exactly in terms of the complex velocity potential [24,29]. The solution allows for nonnormal angles of impingement as well.

For normal impingement, the velocity distribution near the stagnation point can be found by expanding Milne-Thompson's solution [29]. To leading order

$$u_e(x) = \frac{\pi}{4}\left(\frac{u_f}{w}\right)x \tag{13}$$

for x measured along the wall from the stagnation point and w the width of the jet. This approximation is accurate to within 10% for $x/w < 1.1$. It follows that

$$B = 2\frac{w}{u_f}\frac{du_e}{dx}\bigg|_{x=0} = \frac{\pi}{2} \tag{14}$$

Pressure measurements beneath uniform planar waters jet [30,31] are within 10% of those predicted using Eqs. 5 and 13 for $x/w < 1.0$, if jet width and speed are corrected

for the contraction caused by gravitational acceleration. Additional, detailed experimental studies of planar impingement (including nonnormal impact) are described by Schach [24].

Nozzle-to-target effects on B were investigated theoretically by Strand [32] and Miyazaki and Silberman [33]. Analytical solutions for parabolic-profile plane jets were obtained by Sparrow and Lee [34], including nozzle-to-target effects. The corresponding values of B are given in Table 3 and show a significant dependence on l/w.

Wolf et al. [35] studied the effects of velocity nonuniformity in a turbulent, parallel-plate nozzle. For that particular nozzle and Reynolds numbers of 15,000 to 54,000, the centerline velocity was up to 11% higher than bulk velocity. The value of B inferred from wall pressure measurements was roughly 20% greater than for a uniform velocity-profile jet, owing to the nonuniformity of the profile.

3.1.4 Other Cases. The value of B will vary if other velocity profiles are produced by the nozzle employed. The uniform profile and parabolic profile probably provide bounding values for most nozzles.

Downstream variations in the flow field can also alter conditions at the stagnation point. Some evidence suggests that, for low Reynolds number circular jets, viscous boundary layer growth downstream of the stagnation zone may tend to retard the inviscid flow and reduce B, although this conjecture remains unproven. Curvature of the target will also affect B.

3.2 Laminar Boundary Layer Theory

The boundary layer equations along the wall beneath the jet differ slightly for planar and axisymmetric flows. For the planar case, appropriate forms of the equations are

$$\frac{\partial u}{\partial x}+\frac{\partial v}{\partial y}=0 \tag{15}$$

Table 3 Velocity Gradients at the Stagnation Point during Planar Laminar Jet Impingement: $B/2 = (w/u_f)\,(du_e/dx)$; zero surface tension, values from Reference 34

Investigators	$B/2$	Jet type	Inlet velocity profile	l/w
Miyazaki and Silberman [33]	1.93	Planar	Uniform	0.5
	0.890	Planar	Uniform	1.5
	$\pi/4 = 0.785$	Planar	Uniform	∞
Sparrow and Lee [34]	3.48	Planar	Parabolic	0.25
	3.23	Planar	Parabolic	0.375
	3.03	Planar	Parabolic	0.50
	3.03	Planar	Parabolic	1.5

$$u\frac{\partial u}{\partial x}+v\frac{\partial u}{\partial y}=u_e\frac{du_e}{dx}+\nu\frac{\partial^2 u}{\partial y^2} \tag{16}$$

$$u\frac{\partial T}{\partial x}+v\frac{\partial T}{\partial y}=\alpha\frac{\partial^2 T}{\partial y^2} \tag{17}$$

for (u,v) the (x,y) components of velocity. In a cylindrical coordinate system (r,y) with velocity components (u,v), the axisymmetric equations are

$$\frac{\partial(ru)}{\partial r}+\frac{\partial(rv)}{\partial y}=0 \tag{18}$$

$$u\frac{\partial u}{\partial r}+v\frac{\partial u}{\partial y}=u_e\frac{du_e}{dr}+\nu\frac{\partial^2 u}{\partial y^2} \tag{19}$$

$$u\frac{\partial T}{\partial r}+v\frac{\partial T}{\partial y}=\alpha\frac{\partial^2 T}{\partial y^2} \tag{20}$$

These equations are self-similar for appropriate variations of the freestream speed and the wall temperature. Historically noteworthy results for the stagnation zone were published by Hiemenz [20], Homann [21], Goldstein [36], Howarth [22], and Silbukin [37]. For our purposes, it is sufficient to note that the planar flow and energy equations are special cases of the results obtained by Falkner and Skan [38] and Fage and Falkner [39], respectively; the axisymmetric case, after application of Mangler's transformation [40], is also a Falkner flow. White [41] provides a unified discussion of both types of stagnation zone.

For $u_e(x) = Cx$, the planar solutions appear in terms of a stream function ψ and similarity coordinate η:

$$\psi=(\nu x u_e)^{1/2} f(\eta) \tag{21}$$

$$\eta=y\sqrt{\frac{u_e}{\nu x}} \tag{22}$$

$$f'''+f f''=\beta\left(f'^2-1\right) \tag{23}$$

with $\beta = 1$. For the axisymmetric case, with $u_e(r) = Cr$ and an axisymmetric stream function [$u = (1/r)(\partial\psi/\partial y)$, $v = -(1/r)\partial\psi/\partial r)$], there obtains:

$$\psi=\frac{r}{\sqrt{2}}(\nu r u_e)^{1/2} f(\eta) \tag{24}$$

$$\eta = y\sqrt{2\frac{u_e}{\nu r}} \tag{25}$$

where $f(\eta)$ is the solution of Eq. 23 with $\beta = 1/2$. Numerical solutions for $f'(\eta) = u/u_e$ are given for both cases in Table 4 (with boundary conditions $f(0) = f'(0) = 0$ and $f'(\infty) = 1$; data from Reference 42).

Table 4 Velocity Similarity Function $f'(\eta) = u/u_e$ for planar ($\beta = 1$) and Axisymmetric ($\beta = 1/2$) Stagnation Boundary Layers

$\beta = 1$		$\beta = 1/2$	
$f''(0) = 1.2326$		$f''(0) = 0.9278$	
η	$f'(\eta)$	η	$f'(\eta)$
0.0	0.0000	0.0	0.0000
0.1	0.1183	0.1	0.0903
0.2	0.2266	0.2	0.1756
0.3	0.3252	0.3	0.2559
0.4	0.4145	0.4	0.3311
0.5	0.4946	0.5	0.4015
0.6	0.5663	0.6	0.4669
0.7	0.6299	0.7	0.5275
0.8	0.6859	0.8	0.5833
0.9	0.7351	0.9	0.6344
1.0	0.7779	1.0	0.6811
1.1	0.8149	1.1	0.7234
1.2	0.8467	1.2	0.7614
1.3	0.8738	1.3	0.7955
1.4	0.8968	1.4	0.8258
1.5	0.9162	1.5	0.8526
1.6	0.9323	1.6	0.8761
1.7	0.9458	1.7	0.8965
1.8	0.9568	1.8	0.9142
1.9	0.9659	1.9	0.9294
2.0	0.9732	2.0	0.9422
2.2	0.9839	2.2	0.9623
2.4	0.9905	2.4	0.9761
2.6	0.9946	2.6	0.9853
2.8	0.9970	2.8	0.9913
3.0	0.9984	3.0	0.9950
3.2	0.9992	3.2	0.9972
3.4	0.9996	3.4	0.9985
3.6	0.9998	3.6	0.9992
3.8	0.9999	3.8	0.9995
4.0	1.0000	4.0	0.9998

The energy equation is also self-similar for wall temperature variations of the form $(T_w - T_f) = Dx^n$ or Dr^n [39]. If

$$(T_w - T) = (T_w - T_f)\,g(\eta) \tag{26}$$

then we have for either case

$$g'' + \mathrm{Pr}\, fg' - n\,\mathrm{Pr}(2-\beta) f'g = 0 \tag{27}$$

with $g(0) = 0$ and $g(\infty) = 1$. For uniform wall temperature ($n = 0$), the equation can be solved easily:

$$g(\eta) = \frac{\int_0^\eta \exp\left(-\int_0^\eta \mathrm{Pr}\, f(\eta)d\eta\right)}{\int_0^\infty \exp\left(-\int_0^\eta \mathrm{Pr}\, f(\eta)d\eta\right)} \tag{28}$$

The Nusselt number can be calculated directly in terms of g. For planar flows,

$$\mathrm{Nu}_x \equiv \frac{hx}{k} = \left[g'(0)\big|_{\beta=1}\right]\mathrm{Re}_x^{1/2} \tag{29}$$

while for axisymmetric flows:

$$\mathrm{Nu}_r \equiv \frac{hr}{k} = \sqrt{2}\left[g'(0)\big|_{\beta=1/2}\right]\mathrm{Re}_r^{1/2} \tag{30}$$

for $\mathrm{Re}_x = u_e(x)x/\nu$ and $\mathrm{Re}_r = u_e(r)r/\nu$.

Because u_e is linear in x or r, the heat transfer coefficient, h, is independent of x or r. In other words, the thermal boundary layer has a uniform thickness within the stagnation zone. The constant value of h also implies that uniform wall temperature and uniform heat flux boundary conditions are identical. Because the x and r coordinates effectively have no role, we may recast the solutions in terms of the stagnation point velocity gradient:

$$\mathrm{Nu}_w \equiv \frac{hw}{k} = \left[g'(0)\big|_{\beta=1}\right]\mathrm{Re}_w^{1/2}\sqrt{\frac{B}{2}} \tag{31}$$

and

$$\mathrm{Nu}_d \equiv \frac{hd}{k} = \left[g'(0)\big|_{\beta=1/2}\right]\mathrm{Re}_d^{1/2}\sqrt{B} \tag{32}$$

for $\mathrm{Re}_w = u_f w/\nu$ and $\mathrm{Re}_d = u_f d/\nu$.

The function $g'(0)$ can be evaluated numerically at each Prandtl number. Alternatively, curve fits can be used within given ranges of Pr with $n = 0$ [41]. For the planar case:

$$g'(0)\big|_{\beta=1} \approx \begin{cases} \dfrac{\sqrt{2\,\mathrm{Pr}/\pi}}{1+0.64790\sqrt{2\,\mathrm{Pr}/\pi}} & \mathrm{Pr} \le 0.15 \\ 0.57047\,\mathrm{Pr}^{0.4} & 0.15 < \mathrm{Pr} < 3.0 \\ 0.660765(\mathrm{Pr})^{1/3} - 0.076539 & \mathrm{Pr} \ge 3.0 \end{cases} \tag{33}$$

and for the axisymmetric case:

$$g'(0)\big|_{\beta=1/2} \approx \begin{cases} \dfrac{\sqrt{2\,\mathrm{Pr}/\pi}}{1+0.804552\sqrt{2\,\mathrm{Pr}/\pi}} & \mathrm{Pr} \le 0.15 \\ 0.53898\,\mathrm{Pr}^{0.4} & 0.15 < \mathrm{Pr} < 3.0 \\ 0.60105(\mathrm{Pr})^{1/3} - 0.050848 & \mathrm{Pr} \ge 3.0 \end{cases} \tag{34}$$

Other curve fits have occasionally been applied for $0.7 < \mathrm{Pr} < 10$: for planar flow, $g'(0) = 0.57\mathrm{Pr}^{0.37}$; for axisymmetric flow, $g'(0) = 0.54\mathrm{Pr}^{0.37}$.

Equations 31, 32, 33, and 34 provide theoretical expressions for the stagnation-zone heat transfer for any value of B. These equations apply to either uniform wall temperature or uniform heat flux. Power law variations of wall temperature can also be evaluated with Eq. 27. With such solutions, any power series expression for wall temperature can be treated using superposition; some solutions of that type have been published for circular impinging jets by Wang et al. [43]. Wang et al. also examined the impact of the above-negligible radial conduction terms for very abrupt changes in wall temperature.

3.2.1 Boundary Layer Thicknesses. The stagnation point boundary layers are often extremely thin. The 99% momentum boundary layer thickness for planar flow is

$$\frac{\delta}{w} = \frac{3.39}{B^{1/2}\,\mathrm{Re}_w^{1/2}} \tag{35}$$

while that for axisymmetric flow is

$$\frac{\delta}{d} = \frac{2.76}{B^{1/2}\,\mathrm{Re}_d^{1/2}} \tag{36}$$

For example, a 5-mm-diameter, uniform-profile jet at $\mathrm{Re}_d = 6 \times 10^4$ has $\delta = 42$ μm. The thermal boundary layer thickness, δ_t, can be easily estimated from the conduction thickness: $\mathrm{Nu}_d = d/\delta_t$.

4 STAGNATION ZONE NUSSELT NUMBERS

In this section, formulae for calculating the stagnation zone Nusselt number are summarized for both laminar and turbulent unsubmerged liquid jets. Some theoretical aspects of turbulent jets are also discussed. The equations given below should apply for either uniform wall temperature or uniform heat flux situations, although most of the experiments cited were performed as temperature measurements along uniform heat flux surfaces. Properties should be evaluated at the film temperature of $(T_w + T_f)/2$.

4.1 Laminar Jets

The laminar expressions are obtained from the theory laid out in the previous section, specifically Eqs. 31 to 34 with appropriate values of the velocity gradient, B. For a given value of B, these equations, and others in the literature, differ mainly through the curve fit chosen for $g'(0)$.

Comparisons to experiments are described where they are available. The laminar theory generally works quite well when turbulence is eliminated; however, it must be emphasized that turbulence in the impinging jet has been reported to increase the heat transfer coefficient by 30 to 150% beyond that predicted in the following equations.

Nozzle-to-target separation can be expected to influence a laminar jet if: (1) a sharp-edged nozzle is placed too close to the target to complete its contraction, so that a uniform profile is not achieved; (2) if a tube nozzle is placed far enough from the target that viscosity diffuses the parabolic profile toward the bulk velocity; or (3) if the jet velocity is low enough that gravitational acceleration causes significant variation in jet speed and size.

4.2 Laminar Circular Jets

4.2.1 Uniform Velocity-Profile Circular Jets. For uniform velocity profile laminar jets, Liu et al. [9,44] find

$$\mathrm{Nu}_d = 0.745\,\mathrm{Re}_d^{1/2}\,\mathrm{Pr}^{1/3} \tag{37}$$

This result is based on theory and on experiments with cold water. It should apply for all Reynolds numbers above 300 to 400 and for liquids having Prandtl numbers

above 3 or so. The Nusselt number within 10% of the above value for $r/d < 0.7$; at larger radii, the heat transfer coefficient decreases rapidly. The theoretical lead constant is 0.813, but in the above equation it has been adjusted downward (by 9%) to bring it into close agreement with experimental data taken in the range $25{,}000 < \mathrm{Re}_d < 130{,}000$ using long cold water jets and sharp-edged orifice nozzles of 6.3 and 9.5 mm diameter. This equation was found to overpredict Nu_d for water jets of $d_j =$ 2.5 mm by about 15%. A similar equation was given by Nakoryakov et al. [45] for high Prandtl number situations.

For nozzle-to-target separations of less than a few nozzle diameters, a sharp-edged orifice jet is not fully contracted, and the velocity profile is *not* uniform. In that case, heat transfer is likely to be higher than predicted here.

Little data are available for lower Reynolds numbers or for $\mathrm{Pr} < 1$ or $\mathrm{Pr} > 10$. For high Prandtl numbers, the above equation may be used. For Prandtl numbers near unity ($0.15 < \mathrm{Pr} < 3.0$), the theoretical results can be applied to obtain:

$$\mathrm{Nu}_d = 0.729\,\mathrm{Re}_d^{1/2}\,\mathrm{Pr}^{0.4} \tag{38}$$

For $\mathrm{Pr} \ll 1$, as occurs in liquid metal jets, theory yields:

$$\mathrm{Nu}_d = 1.08\,\mathrm{Re}_d^{1/2}\,\mathrm{Pr}^{1/2} \tag{39}$$

Convective heat transfer coefficients for liquid metal jets are typically 3 to 8 times greater than those for water jets of the same diameter size and speed. Such jets may have value in applications for which very high h is required; for example, jets of liquid gallium are being considered for use in cooling high energy synchrotron X-ray components [46,47].

4.2.2 Parabolic Velocity-Profile Circular Jets. For jets issuing from tubes long enough to produce a fully developed laminar flow, the velocity profile is parabolic if the Reynolds number is below the transition value of 2000 to 4000. Theory and experimental data by Scholtz and Trass [28] show

$$\mathrm{Nu}_d = 1.648\,\mathrm{Re}_d^{1/2}\,\mathrm{Pr}^{0.361} \tag{40}$$

This equation should apply for $1 < \mathrm{Pr} < 10$ and Reynolds numbers ranging from 100 to 200 up to 2000 to 4000. This equation is in good agreement with sublimation experiments for $\mathrm{Pr} = 2.45$ and $500 < \mathrm{Re}_d < 1960$, and it appears to be unaffected by nozzle-to-target separation for $0.05 < l/d < 6$.*

* Submerged air jets between 19 and 51 mm diameter were used; l/d was small enough for these jets to behave as unsubmerged jets near the stagnation point.

The size of the uniform-h stagnation zone for this case is roughly $r/d < 0.15$, but the Nusselt number is within 10% of the stagnation-point value for $r/d < 0.4$; beyond this radius, the Nusselt number usually decreases sharply. An exception occurs when $l/d \le 0.1$, for which case Nu_d can actually increase with r/d as the edge of the nozzle is approached.

4.2.3 Other Laminar Velocity Profiles. Other laminar nozzles may produce profiles intermediate to the uniform and parabolic cases, depending, for example, on the state of flow development associated with the nozzle's entry length. If the value of the dimensionless gradient B is known, the theoretical results of the preceding section may be applied. Otherwise, the values of h for uniform and parabolic jets may be used as lower and upper bounds, respectively.

4.3 Laminar Planar Jets

A limited body of experimental data is available for laminar planar jets. Some theoretical equations and the experimental results are as follows.

4.3.1 Uniform Velocity-Profile Planar Jets. Uniform velocity-profile planar laminar jets can be produced by sharp-edged slot nozzles [6]. For $0.7 < \mathrm{Pr} < 10$, Inada et al. [31] recommend the theoretical equation

$$\mathrm{Nu}_w = 0.505\,\mathrm{Re}_w^{1/2}\,\mathrm{Pr}^{0.376} \tag{41}$$

which shows good agreement with a long laminar water jet experiment at $\mathrm{Re}_w = 920$. They point out that their experiments with a turbulent water jet lie 70 to 80% above this equation. The Nusselt number is within 10% of this value for $x/w < 0.8$.

For uniform-profile liquid metal jets ($\mathrm{Pr} \ll 1$), a theoretical equation is

$$\mathrm{Nu}_w = \frac{1}{\sqrt{2}}\,\mathrm{Re}_w^{1/2}\,\mathrm{Pr}^{1/2} \tag{42}$$

4.3.2 Parabolic Velocity-Profile Planar Jets. For parabolic velocity profile jets, such as produced by a long parallel-plate channel with Reynolds numbers below transition, the theoretical Nusselt number is

$$\mathrm{Nu}_w = 0.993\,\mathrm{Re}_w^{1/2}\,\mathrm{Pr}^{0.4} \tag{43}$$

in the range $0.15 < \mathrm{Pr} < 3$ with $l/d = 1.5$. A result of this general form was compared by Sparrow and Lee [34] to the sublimation data of Sparrow and Wong [48] for a 12:1

rectangular laminar jet; the prediction is about 10% above the data for Reynolds numbers between about 500 and 2000, but the deviation was attributable to axial variations of the nozzle velocity profile. The stagnation-zone result is applicable for $x/w < 0.3$.

4.3.3 Other Laminar Planar Jets. Garg and Jayaraj [49] published numerical solutions for uniform-profile slot jets at nonnormal angles of impingement. Their results show that stagnation-point Nusselt numbers can be 2 to 4 times larger at acute angles of impingement, but that the width of the stagnation zone is also greatly reduced.

Additional formulae for laminar planar jets may be obtained by manipulation of the theoretical results discussed in Section 3.

4.4 Turbulent Liquid Jets

The manifolding and piping systems that supply liquid to nozzles are often turbulent, and, unless the nozzle has a very high contraction ratio, this turbulence will be carried into the jet formed. A jet issuing from a fully developed tube flow without a terminating nozzle will also be turbulent if the Reynolds number is above about 4000. Turbulent jets have elevated heat transfer coefficients owing to both the direct effect of freestream turbulence on the stagnation-point boundary layer and the more indirect effect of a nonuniform velocity profile on the stagnation-point velocity gradient. The increases relative to laminar theory may range from 30 to 150%.

4.4.1 Velocity Profile Effects. In contrast to laminar velocity profiles, which typically vary from uniform to parabolic (with u_{max}/u_f up to 2), the velocity profiles of turbulent jets will likely vary between a uniform distribution and the mildly nonuniform distributions typical of fully developed turbulent flows. In the latter case, however, the centerline velocity may still be significantly greater than the bulk velocity. For example, at a Reynolds number of 4000 in a circular tube, $u_{max}/u_f = 1.27$, and at $\mathrm{Re}_d = 10^5$, $u_{max}/u_f = 1.18$.

In this connection, the measurements of Stevens et al. [50] are relevant. They made laser-doppler measurements of the radial velocity gradient for several turbulent-flow nozzles located a distance of one nozzle diameter from a target. For a contoured, converging nozzle, the gradient found was $B \approx 2.3$. This particular nozzle would be expected to have the most nearly uniform velocity profile, and its stagnation-point gradient is near the uniform-profile theoretical value of $B = 1.831$. For laminar heat transfer, this difference in gradients would cause the contoured nozzle's Nusselt number to exceed that of a uniform profile by about 12%. Corresponding measurements for a fully developed pipe nozzle showed $B = 3.6$ at $l/d = 1$ [51], well above the uniform value; this difference would increase laminar heat transfer by 41%. One may conclude that variations in B among nozzles can have significant effects on turbulent jet heat transfer when the nozzle-to-target spacing is small.

However, all jets will approach a uniform velocity profile at the bulk velocity when l/d increases, because viscosity tends to elminate radial gradients. Stevens and Webb [13] found that the bulk velocity was typically reached within about five diameters downstream of the nozzle. For long jets, one might infer that $B \rightarrow 1.83$ (uniform profile) and that the observed increases in heat transfer for long jets result mainly from turbulence effects.

4.4.2 Turbulence Effects. The stagnation-zone boundary layer is likely to remain laminar at the jet Reynolds numbers of interest, but turbulence in the impinging jet will tend to disrupt this very thin boundary layer, raising the heat transfer coefficient. This effect is very well documented for the stagnation zone of bodies in gas flows. For example, correlations for the stagnation-zone enhancement have been made [52-54], and the effect has been clearly documented in gas-jet impingement [55], including time-resolved measurements of the turbulent heat flux [56]. That literature has been summarized by Vader et al. [57].

The correlations for turbulence enhancement generally add polynomial terms in $(\mathrm{Tu} \cdot \mathrm{Re})$ to the laminar stagnation Nusselt number for the gas flow, where Tu is the freestream turbulence intensity (e.g., u'/u_f). Thus, if Tu can be estimated, the Nusselt number is obtained by a modification of the laminar theory. These correlations also show that the impact of a nonzero Tu increases as the Reynolds number increases.

In contrast, few controlled studies of freestream turbulence are available for Prandtl numbers above unity (or well below unity), and no correlations or quantitative theory for Tu effects in those ranges of Pr are known to the author. Unfortunately, many applications of impinging liquid jets involve these Prandtl number ranges: general purpose cold-water jets with $2 < \mathrm{Pr} < 10$; fluorocarbon jets with $10 < \mathrm{Pr} < 70$ for electronics cooling; oil jets with $\mathrm{Pr} > 100$ for some electrical and machine-tool cooling applications; and liquid-gallium jets with $\mathrm{Pr} \approx 0.026$ for cooling synchrontron X-ray components.

Most turbulent liquid jet experiments are based on water jets with Prandtl numbers between 2.5 and 9, and the turbulence levels associated with liquid-jet heat transfer data have been measured in only one or two studies. The associated correlations have usually fit data to the form suggested by laminar theory, adjusting the lead constant and Reynolds number exponent as necessary. The Prandtl number exponent is generally chosen on the basis of the laminar curve-fits to $g'(0)$. Thus, the independent effects of Tu, Pr, and Re are lumped together in such results to produce simple engineering equations.

In consequence, the available correlations for turbulent jet Nusselt number are likely to differ from design conditions if changes in the manifolding or nozzle arrangements increase or decrease the turbulence level relative to the experiments, or if the Prandtl number range is substantially different than the conditions of the experiments considered. Existing data do not clearly bound the expected variations; however, changes in turbulence level are probably less important than changes in B for Reynolds numbers below 50,000. Above 50,000, Tu variations are likely to have

increasing impact. Roughly speaking, any variations will amount to tens of percent, rather than orders of magnitude.

One well-defined turbulent condition is a fully developed turbulent flow, as issues from a tube or channel of more than about 40 diameters in length. Turbulence intensities for such channel flows are generally 4 to 5% in the core of the flow. Several investigators have adopted such nozzles as a standard for turbulent jets. Other nozzles, which may often have a strong and well-contoured contraction, are likely to exhibit less turbulence than this, although they are unlikely to be entirely laminar unless particular care is taken in the manifolding and in the deliberate selection of a suitably high contraction ratio. If, on the other hand, the nozzle has a flow separation within it, the turbulence level could be significantly higher than for fully developed flow.

For purposes of stagnation-zone heat transfer enhancement, a higher turbulence level may be desirable. Internally roughened nozzles (e.g., Figure 2e) can provide turbulence without the added length required to establish fully developed flow; at present, however, no quantitative design data is available for such nozzles. Hydrodynamically, turbulent jets have the drawback of smaller breakup lengths and a tendency to splatter. These factors must be weighed if the design configuration calls for a jet of more than a few diameters in length.

4.4.3 Separating Turbulence and Velocity Gradient Effects. The study by Stevens et al. [50] and by Pan et al. [58] is interesting in this regard. These investigators used four different nozzles that produced four different velocity gradients and four different turbulence intensities in water jets issuing from a turbulent plenum at $l/d = 1$. Nusselt numbers were measured for $16{,}600 < \mathrm{Re}_d < 43{,}700$. The velocity gradients ranged from $B = 2.3$ to $B = 4.4$ and the freestream turbulence intensities ranged from 2 to 13%. Corresponding stagnation-point Nusselt numbers differed by 40 to 50% at fixed Reynolds number.

The values of B and Tu were not entirely independent in these experiments. Nonetheless, the results showed a much stronger correlation of the Nusselt number with the size of B than with the size of Tu. Moreover, if the correlation that was obtained is compared with the laminar prediction using the measured values of B, the Nusselt numbers agree to within a few percent. These striking results suggest a relatively weak influence of freestream turbulence in the range of Reynolds number studied.

This conclusion must be tempered with the recognition that freestream turbulence effects generally increase in importance as Reynolds number increases. Indeed, water jet data at higher Reynolds number suggest an increasing turbulence effects: the Reynolds number dependence of Nu_d apparently becomes stronger when Re_d increases past a threshold value. This type of change has been observed by both Faggiani and Grassi [59] and by Gabour and Lienhard [60].

4.4.4 Nozzle-to-Target Separation Effects. Velocity gradients, as discussed above, vary with the nozzle-to-target separation. The turbulence intensity in the jet should also vary with l/d, as a result of both viscous dissipation of the turbulence and the

increasing disturbances on the surface of the jet (see Section 6.1); the net change in turbulent fluctuation may well be an increase, given the strong evolution of the rms liquid surface roughness. For low-speed jets, gravitational acceleration can cause speed and diameter to vary with l/d, changes whose size can be estimated (see Section 2.1).

The effect of varying nozzle-to-target separation has been examined in several experiments [59-61]. Collectively, these studies have measured the stagnation-point Nusselt number of fully developed turbulent water jets for l/d between 1 and 33 and Reynolds numbers between 9000 and 130,000. The results show that l/d has almost no influence for $l/d > 5$ to 10. The data suggest that, for Reynolds numbers below about 25,000, decreasing l/d from a large value down to unity may raise Nusselt number by up to 15%. For higher Reynolds number, the variation with l/d is within the scatter of the data.

4.4.5 Wall Conduction Limitations. High Reynolds number turbulent jets can produce very high heat transfer coefficients, and typical values may easily exceed 100 kW/m^2. Consequently, the conduction resistance of the target surface can limit the heat transfer, even for a relatively thin, metallic surface. Designers should allow for conduction effects in any liquid jet impingement system. Analytical studies of such conjugate heat transfer have been made by Wang et al. [62,63].

For experimentalists building correlations, this difficulty affects the evaluation of liquid-side wall temperature when an electrically heated sheet (of thickness t and conductivity k_w) is used as the test surface and temperature is measured on its dry backside. The temperature drop through the heater is $\Delta T = q_w t/2k_w$. If this correction is omitted in calculating the Nusselt number, the value of Nu_d obtained can be low. This error increases with Reynolds number, and, in typical experimental systems, it can lower Nu_d by 1/3.

4.5 Turbulent Circular Jets

Circular jets issuing from long tubes will have fully developed turbulent flow for Reynolds numbers above a transition value of 2000 to 4000.

For $4000 < \mathrm{Re}_d < 52000$, Stevens and Webb [61] correlated

$$\mathrm{Nu}_d = 1.51\,\mathrm{Re}_d^{0.44}\,\mathrm{Pr}^{0.4}(l/d)^{-0.11} \tag{44}$$

to an average error of 15% and a maximum error of 60%. For $16600 < \mathrm{Re}_d < 43700$, Pan et al. [58] recommend the following correlation for nozzles whose stagnation-point velocity gradient is known:

$$\mathrm{Nu}_d = 0.49\,\mathrm{Re}_d^{1/2}\,\mathrm{Pr}^{0.4}\,B^{1/2} \tag{45}$$

These results are both based on cold water jets; the given Prandtl number exponents are assumed, but might be expected to apply in general range of 1 to 10. The

stagnation zone, of constant Nu_d, is roughly $r/d < 0.7$. For a fully developed tube nozzle at $l/d = 1$, $B \approx 3.6$, and the second equation becomes

$$Nu_d = 0.92\,Re_d^{1/2}\,Pr^{0.4} \tag{46}$$

for $16600 < Re_d < 43700$ to an accuracy of about 5%.

At higher Reynolds number, both Gabour and Lienhard [60] and Faggiani and Grassi [59] report a stronger dependence of Nusselt number on Reynolds number. This may result from an increasing influence of freestream turbulence; however, further evidence is needed to verify that conjecture. Faggiani and Grassi provide low Reynolds-number correlations that are in general agreement with Stevens and Webb for Re_d below about 43,000. For higher Reynolds numbers, their Nusselt number correlations are below Gabour and Lienhard's by up to 37%, but this difference may be associated with conduction corrections in the measured wall temperature that only become significant at high Reynolds number. If such corrections are applied to Faggiani and Grassi's reported results, those results become quite close to those of Gabour and Lienhard.* Alternatively, these differences may result from other differences between the two experiments, possibly related to turbulence structure or jet size: Faggiani and Grassi used a much larger jet than Gabour and Lienhard.

For $25{,}000 < Re_d < 85{,}000$, Gabour and Lienhard obtain

$$Nu_d = 0.278\,Re_d^{0.633}\,Pr^{1/3} \tag{47}$$

based on experiments with cold water jets having $8.2 < Pr < 9.1$ and tube diameters between 4.4 and 9.0 mm. The uncertainty of the data (at a 95% confidence level) is less than ±10%. Gabour found that the effect of changing l/d between 1 and 20 was within the uncertainty of the data. The assumed Prandtl number exponent is appropriate for $Pr > 3$.

Figure 8 shows the stagnation-zone Nusselt number of fully developed circular jets for $500 < Re_d < 10^5$ and Pr = 8, as predicted by Eqs. 40, 44, and 47. (Eq. 46 is quite close to those shown, and l/d was set to 1 in Eq. 44. The Nusselt number for a sharp-edged orifice nozzle (Eq. 37) is also shown.

4.6 Turbulent Planar Jets

Several recent studies have investigated turbulent planar jet cooling in the stagnation zone.

Vader et al. [57,64] and Zumbrunnen et al. [30] used highly converging nozzles to produce uniform velocity-profile water jets. These nozzles were intended to

* It should be noted that Gabour's experiments were conducted with an awareness of the disagreements and that particular pains were taken to verify all calibrations.

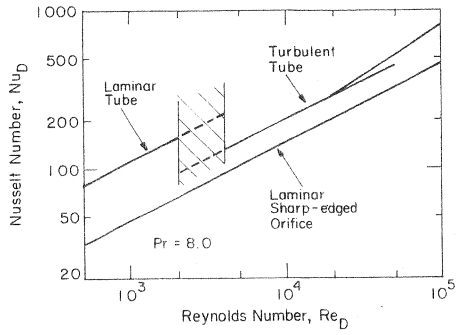

Figure 8 Stagnation-zone Nusselt number for circular liquid jets at Pr = 8.

suppress, but not eliminate, turbulence; presumably, the jets had an rms intensity of less than a few percent. The stagnation-zone results were correlated as

$$Nu_w = 0.28\,Re_w^{0.58}\,Pr^{0.4} \tag{48}$$

based on Re_w 20,000 to 90,000 and Pr between 2.7 and 4.5. The Nusselt numbers had decreased by about 10% at $x/w = 1.0$. These jets ran at fairly low speed, and, consequently, corrections for gravitational acceleration were applied in estimating the jet width and speed from the nozzle width and speed. The heat transfer coefficients were 30 to 50% above laminar theory, apparently owing to residual turbulence in the jet.

Wolf et al. [35] used a long parallel-plate nozzle to produce fully developed turbulent jets. They correlated their results to an accuracy of 10% as

$$Nu_w = 0.116\,Re_w^{0.71}\,Pr^{0.4} \tag{49}$$

based on Re_w from 17,000 to 79,000 and Pr between 2.8 and 5.0. The stagnation zone of uniform Nu_d extended to roughly $x/w < 0.5$. Expected turbulence intensities for such a flow would be on the order of 4 to 5%; the measured centerline velocity was as much as 11% above the bulk velocity. Note that the heat transfer coefficients were up to 79% above that for the uniform jet of Vader et al.

4.7 Other Turbulent Liquid Jets

4.7.1 Turbulent Liquid-Metal Jets. For liquid-metal jets, the impact of freestream turbulence is quite possibly small, owing to the high molecular conductivity relative to the turbulent eddy diffusivity. In the absence of other information, the laminar results above may be applied to such jets, although turbulence will likely increase the heat transfer coefficient as the Reynolds number increases. Data for turbulent liquid metal heat transfer are limited [65], however, and this recommendation is somewhat speculative.

4.7.2 Turbulent Circular Jets Impinging on Rough Walls. The very thin boundary layer of the stagnation zone can be disrupted by even small levels of wall roughness. Gabour and Lienhard [60] measured the stagnation-point Nusselt number for fully developed turbulent cold-water jets impinging on surfaces of varying roughness. They found that roughness of only 28 μm rms height could raise the Nusselt number by up to 50%.

For those experiments, mild steel (1010) surfaces were scored in a cross-hatch pattern. The depth of scoring was varied to yield a range of rms roughness, $4.7 < k < 28.2$ μm, while holding the pattern of roughness fixed. Measurements were made for nozzles of diameter $d = 4.4$, 6.0 and 9.0 mm and Reynolds numbers from 20,000 to 84,000. The Prandtl number was held between 8.2 and 9.1. Roughness effects on the Nusselt number depended on Re_d and the dimensionless roughness $k^* = k/d$, as shown in Figures 9 and 10. On these figures, the lowest curves ($k^* < 0.0008$) are effectively smooth walls; for higher k^*, the Nusselt number is greater than for a smooth surface, and the enhancement rises with Re_d. Figure 10 shows curve fits to the experimental data that can be used to estimate the effect of roughness and Reynolds number on Nusselt number at Prandtl numbers in the range of 8 to 9.

Gabour and Lienhard constructed a curve fit for the threshold level of roughness at which the Nusselt number is increased by 10%:

$$k^* = 5.95\,\mathrm{Re}_d^{-0.713} \tag{50}$$

For lower levels of roughness (smaller k^*), the surface can be viewed as smooth. No data are yet available for different Prandtl numbers; however, Gabour and Lienhard proposed on the basis of boundary layer arguments that the threshold can be estimated for Prandtl numbers above unity as:

$$k^* = 12.1\,\mathrm{Re}_d^{0.713}\,\mathrm{Pr}^{-1/3} \tag{51}$$

In applying these results, it must be remembered that: (1) roughness effects usually vary with the geometry of the roughness, not only with its height; (2) the Prandtl number will undoubtedly have an important influence, presumably making higher Prandtl number jets more susceptible to roughness effects; (3) the wall material can be expected to play a role in roughness effects, especially for lower wall conductivity and higher Nusselt numbers; and (4) the overall scaling of stagnation-point wall roughness is different than for standard boundary layers and pipe flows, owing to the nearly zero shear stress of the stagnation zone, and this scaling is as yet unknown.

Some related data are given by Sullivan et al. [66], who examined the use of heavily roughened spreader plates for jet-impingement cooling of electronics. The total thermal resistance of the spreader plate and jet was measured, reflecting both the conduction resistance of the spreader and the area-averaged heat transfer coefficient along its surface. The roughness employed was an order of magnitude larger than that

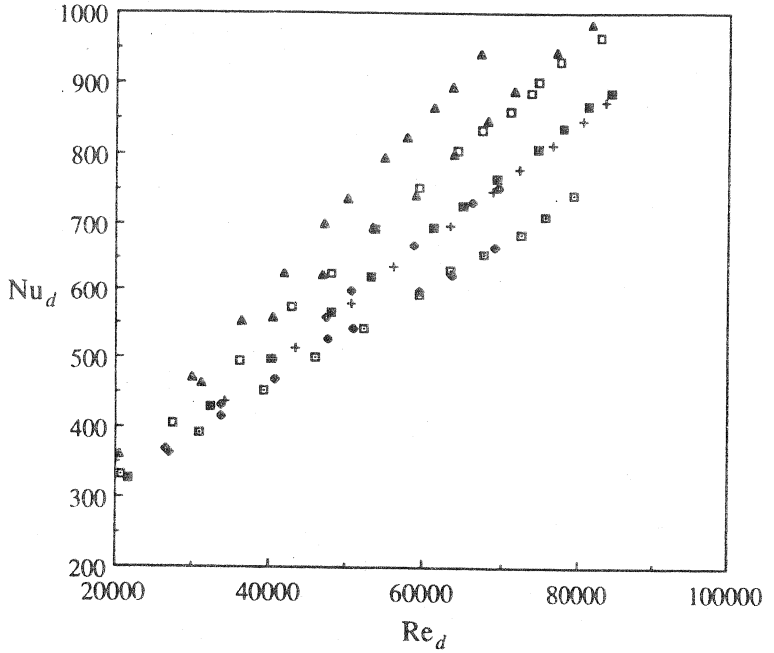

Figure 9 Wall roughness effects on stagnation-zone Nusselt number for circular turbulent liquid jets at Pr = 8-9 (data from [60]).

of Gabour and Lienhard. Sullivan et al. showed that roughness could produce a substantial decrease in overall thermal resistance (viz., an increased average h), and that this effect increased with Reynolds number. The trends were qualitatively similar to those described above.

4.7.3 Inclined Turbulent Jets. Measurements for circular turbulent jets at nonnormal angles of impact are given by Stevens and Webb [67]. Data for inclined planar jets are given by McMurray et al. [68]. Each paper reports an asymmetry of the local Nusselt number about the stagnation point, with a more rapid decrease of Nu_d along the upstream direction than the downstream direction.

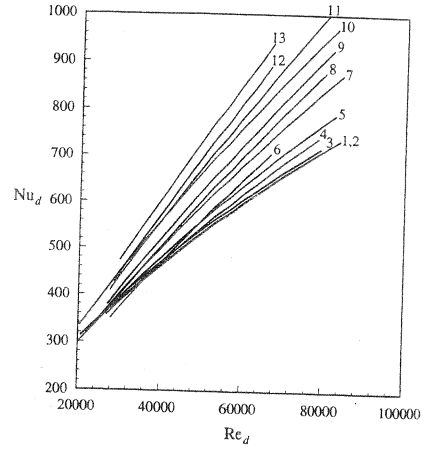

Figure 10 Wall roughness effects on stagnation-zone Nusselt number for circular turbulent liquid jets at Pr = 8 – 9. Curve fits for the following roughness: 1, k* = 0.00005; 2, k* = 0.00052; 3, k* = 0.00074; 4, k* = 0.00103; 5, k* = 0.00147; 6, k* = 0.00195; 7, k* = 0.00229; 8, k* = 0.00293; 9, k* = 0.00323; 10, k* = 0.00437; 11, k* = 0.00464; 12, k* = 0.00596; 13, k* = 0.00641 [60].

5 LOCAL HEAT TRANSFER DOWNSTREAM

The flow downstream of the stagnation zone is characterized by growing boundary layers and a decreasing heat transfer coefficient. For both planar and axisymmetric jets, the boundary layers are laminar near the stagnation zone and undergo a turbulent transition farther downstream. Transition produces a local increase in the heat transfer coefficient, again followed by a declining trend. If the incoming jet is turbulent, local h upstream of transition can be increased, especially in the accelerating flow near the stagnation zone; and the location of turbulent transition is moved upstream. Far downstream, the impinging jet flow may be terminated by a hydraulic jump whose location depends on both upstream and downstream flow conditions.

Beyond these general features, however, planar and axisymmetric jets differ substantially. A planar jet divides at the stagnation line, and the inviscid flow downstream has half the thickness of the incoming jet and moves at the jet's velocity (Figure 11). The boundary layers grow as they might under any variable speed

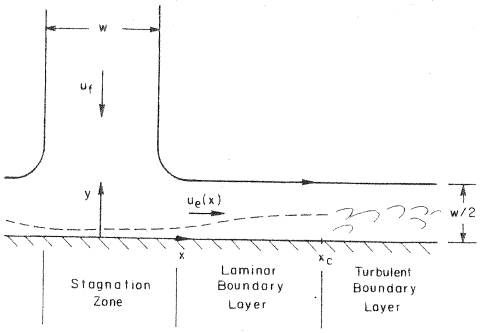

Figure 11 Downstream development of a planar impinging jet.

freestream flow, and, if the jet Reynolds number is not too low, the boundary layers can remain thin relative to the overlying liquid sheet.

Axisymmetric jets, in contrast, are spread thinner as they travel radially outward (Figure 12). The flow perimeter increases as $2\pi r$, and inviscid mass conservation requires the liquid sheet thickness to decrease as $h(r) = d^2/8r$. This rapid decrease quickly brings the growing boundary layer into contact with the surface of the liquid sheet, transforming the flow from a boundary layer into a high-momentum viscous film with a radially increasing bulk temperature. Thus, analysis and correlation of circular jet heat transfer becomes far more complicated than for planar jets, owing to radial changes in the heat transfer mechanism. In addition, any incoming turbulence in the axisymmetric jet can greatly disturb the free surface of the thin liquid sheet, causing splattering of the liquid and a very rapid transition to a turbulent film flow.

In this section, downstream evolution is described for laminar and turbulent planar jets and for laminar axisymmetric jets. The downstream heat transfer of turbulent axisymmetric jets is addressed separately in Section 6, following an examination of the phenomenon of splattering. Hydraulic jump processes are discussed briefly at the end of the present section.

5.1 Planar Jets

Theoretical results are available for uniform velocity profile planar jets. Only a little experimental data are available for laminar planar jets; most other data apply to planar jets with some level of turbulence present.

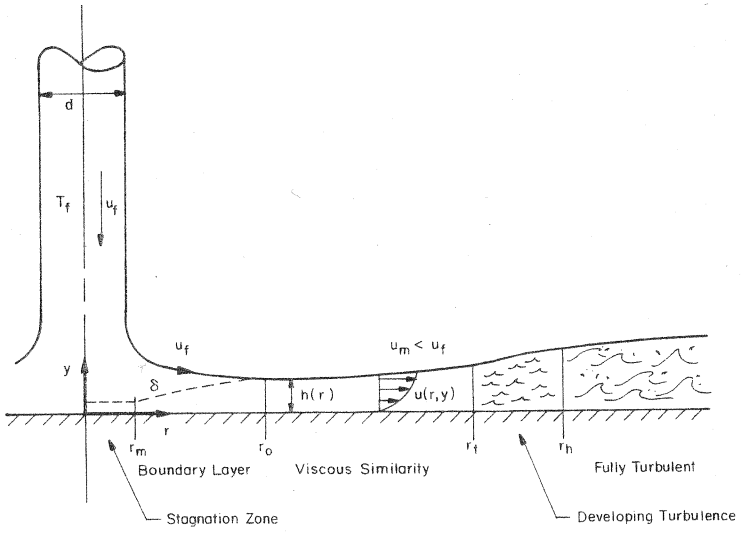

Figure 12 Downstream development of an axisymmetric impinging jet.

5.1.1 Laminar Planar Jet Results. The planar boundary layers are described by Eqs. 15 to 17, but the inviscid flow now tends toward a constant speed, u_f, with increasing x. Vader et al. [57] showed that the inviscid velocity could be approximated as

$$\frac{u_e(x)}{u_f} = \frac{\pi}{4}\left(\frac{x}{w}\right), \quad 0 \le x/w \le 1 \tag{52}$$

$$\frac{u_e(x)}{u_f} = \tanh\left(\frac{x}{w}\right), \quad x/w > 1 \tag{53}$$

with a maximum error of 5% occurring near $x/w = 1$. Alternatively, the previously mentioned exact solution [29] can be used. With $u_e(x)$, the laminar boundary layer equations can be integrated directly.

Garg and Jayanta [49] solved the boundary layer equations numerically, using the exact freestream velocity. They gave graphical results for local and mean Nusselt numbers over a limited range of parameters for isothermal targets.

Inada et al. [31] instead approximated the flow with the Falkner-Skan solutions at the local value of the pressure gradient, which was calculated from the exact freestream solutions. They obtained expressions for the local Nusselt number that could be evaluated using their graph of a local pressure-gradient parameter. The resulting solutions are somewhat cumbersome to reproduce here, but they showed good agreement with experimental data for a jet striking a uniform heat flux target for a Reynolds number of 940 in the range $x/w < 2.5$. As the freestream speed tends to u_f at large x/w, their equation limits to:

$$\mathrm{Nu}_w = 0.4610\,\mathrm{Re}_w^{1/2}\,\mathrm{Pr}^{0.34}\left(\frac{w}{x}\right)^{1/2} \tag{54}$$

(within 10% for $x/w > 2.0$). If written in terms of Nu_x, this equation is seen to be the usual result for a constant heat flux, flat plate boundary layer. Inada et al. also give expressions for uniform wall temperature targets.

Inada et al. found that variations in nozzle-to-target separation had a significant effect on Nu_w in the stagnation zone when the nozzle was within about 0.5 w of the target, but had little effect for greater separations. This behavior is similar to that predicted by Scholtz and Trass [28] for the stagnation zone. For $x/w > 1.5$ or so, nozzle spacing had little effect on the local Nusselt number for any nozzle separation.

5.1.2 Turbulent Planar Jet Results. Turbulence is present in most planar jets, and heat transfer rates downstream are generally higher than the laminar analysis predicts. Experiments using nozzles with low levels of turbulence have been performed by McMurray et al. [68], Zumbrunnen et al. [30], and Vader et al. [57].

The correlation of Vader et al. (for the slightly turbulent nozzle of nearly uniform profile described in Section 4.6) is typical of the results of those studies:

$$\mathrm{Nu}_x = 0.89\,\mathrm{Re}_x^{0.48}\,\mathrm{Pr}^{0.4} \tag{55}$$

This equation uses a Reynolds number, $\mathrm{Re}_x = u_e(x) \cdot x/\nu$, based on the local freestream velocity from Eqs. 52, 53. It applies to uniform heat flux surfaces for $100 < \mathrm{Re}_x < \mathrm{Re}_{x,c}$, where $\mathrm{Re}_{x,c}$, is the turbulent transition Reynolds number. Physical properties are evaluated at $(T_w + T_f)/2$, and the data on which the correlation is based were obtained using water jets. This result is on the order of 60 to 70% above the prediction of laminar theory. McMurray et al. obtained a correlation that is very close to this one.

For $\mathrm{Re}_x < 100$, Vader et al. recommend that a stagnation-zone correlation be used. Note that this range of Re_x corresponds to

$$\frac{x}{w} < \frac{20}{\sqrt{\pi}}\mathrm{Re}_w^{-1/2} \tag{56}$$

The values of x/w obtained from Eq. 56 lie in the portion of the stagnation zone for which some decrease in h with x occurs. On the other hand, the stagnation-zone Nusselt number correlations are themselves accurate to about 10% for $x/w < 1$.

The heat transfer coefficient begins to increase with x when turbulent transition starts, reaching a maximum when transition is complete. Thereafter, the heat transfer coefficient again declines with increasing x. Turbulent transition thus produces a local peak in the heat transfer coefficient, and data for planar jets show that this peak can be similar in amplitude and breadth to that of the stagnation zone. Turbulent transition for the planar jet was reported by Vader et al. to begin at $\mathrm{Re}_{x,c} = 3.6 \times 10^5$ (in nonboiling flow), and McMurray et al. obtained the same value. The transition Reynolds number will, of course, vary with the level of disturbances present in any particular jet impingement system.

In the turbulent region, McMurray et al. recommend the following correlation:

$$\mathrm{Nu}_x = 0.037\,\mathrm{Re}_x^{0.8}\,\mathrm{Pr}^{1/3} \tag{57}$$

This equation is supported by data for $6 \times 10^5 < \mathrm{Re}_x < 2.5 \times 10^6$.

Fully developed turbulent planar jets were used in a study by Wolf et al. [35]. As previously described (Section 4.6), the velocity profile for these jets is more nonuniform and more turbulent than for the jets of Vader et al. and of McMurray et al., and substantially higher stagnation-zone heat transfer coefficients were obtained. Turbulent boundary layer transition occurred farther upstream than for the weakly turbulent uniform profile jets, and the heat transfer was considerably greater at all positions on

the wall. For x/w upstream of turbulent transition, Wolf et al. correlated their local heat transfer coefficient data for water jets as

$$\mathrm{Nu}_w = \mathrm{Re}_w^{0.71}\,\mathrm{Pr}^{0.4}\, f(x/w) \tag{58}$$

where

$$f(x/w) = \begin{cases} 0.116 + (x/w)^2\,[0.00404(x/w)^2 - 0.00187(x/w) - 0.0199], & 0 < x/w < 1.6 \\ 0.111 - 0.0200(x/w) + 0.00193(x/w)^2, & 1.6 < x/w < 6 \end{cases} \tag{59}$$

The correlation applies to $1.7 \times 10^4 < \mathrm{Re}_w < 7.9 \times 10^4$ and is accurate to 9.6% at a 95% confidence level.

5.2 Laminar Axisymmetric Jets

5.2.1 Flow Field. A laminar axisymmetric jet creates a radial film that evolves as shown in Figure 12. The thickness of the liquid sheet initially decreases with radius (as $1/r$), but, because viscous drag slows the liquid sheet, its thickness begins to increase at larger radii. The flow field may be divided into successive regions:

1. The stagnation zone.
2. The laminar boundary layer region, in which the viscous boundary layer thickness, δ, is less than the thickness of the liquid sheet, $h(r)$, and the rest of the liquid sheet moves at the incoming jet's speed, u_f. The flow is now nearly parallel to the wall.
3. The viscous similarity region, in which viscous effects extend through the entire liquid film [$\delta = h(r)$]. In this region, the surface speed, u_m, decreases with increasing radius.
4. The region of developing turbulence.
5. The region of fully turbulent flow. This region may relaminarize farther downstream, as the film speed decreases.

Theoretical solutions for the boundary layer and viscous similarity region were first obtained by Watson [69]. Watson's analysis of the boundary layer region led to a Blasius type similarity solution for $\delta < h(r)$. In the region where $\delta = h(r)$, Watson obtained an elegant similarity solution that encompasses the entire thickness of the liquid sheet. Watson also obtained solutions for a turbulent film flow and for the hydraulic jump; however, these solutions are somewhat unsatisfactory, as discussed by Liu et al. [44] and by Liu and Lienhard [70].

Watson's laminar results were experimentally substantiated by Azuma and Hoshino [71-75] using laser-doppler measurements. (An earlier, and negative, experimental test by Olsson and Turkdogan [76] was probably too crude to be reliable.) Azuma and Hoshino used an annular orifice mounted onto the plate, rather than an actual impinging jet. Their velocity profiles showed good agreement to Watson's in the laminar regions of the flow, although somewhat better agreement could be obtained using a quartic polynomial approximation to the velocity profile in the boundary layer region; the measurements converged to Watson's similarity solution farther downstream. Sharan [77] independently obtained approximate integral-method solutions for both regions, and Wang et al. [78] developed a series solution for the boundary layer region.

The various analytical studies are in relatively good agreement with one another, in spite of minor differences in the approximations they employ. To reasonable accuracy, the integral-method results can be used [44,77,79], as we now summarize.

The region of boundary layer behavior, with $u_m(r) = u_f$, begins at $r \approx 2.23\ d$. In this region, the boundary layer thickness is approximately

$$\delta = 2.679\left(\frac{rd}{\mathrm{Re}_d}\right)^{1/2} \tag{60}$$

and the velocity profile is approximately:

$$u(r,y) = u_m(r)\left[\frac{3}{2}\frac{y}{\delta} - \frac{1}{2}\left(\frac{y}{\delta}\right)^3\right] \tag{61}$$

The viscous boundary layer reaches the surface of the liquid sheet at a radius r_o given by:

$$r_o = 0.1773\,\mathrm{Re}_d^{1/3} d \tag{62}$$

Beyond r_o the free surface speed decreases as:

$$u_m(r) = \frac{1}{5}\frac{u_f d^2}{h(r) r} \tag{63}$$

where the liquid sheet thickness is

$$h(r) = 0.1713\left(\frac{d^2}{r}\right) + \frac{5.147}{\mathrm{Re}_d}\left(\frac{r^2}{d}\right) \tag{64}$$

For $r > r_o$, the velocity profile may be obtained from the polynomial approximation (Eq. 61) with u_m from Eq. 63 and $\delta = h(r)$ from Eq. 64.

The radius of onset of turbulence, r_t, was correlated by Azuma and Hoshino [72] as

$$\frac{r_t}{d} = 730\,\mathrm{Re}_d^{-0.315} \tag{65}$$

and by Liu et al. [44] as

$$\frac{r_t}{d} = 1200\,\mathrm{Re}_d^{-0.422} \tag{66}$$

These results are compared in Figure 13; the difference probably results from the individual characteristics of the experimental systems. Liu et al. inferred from heat transfer data the radius at which turbulence became fully developed, and correlated it as:

$$\frac{r_h}{d} = 28600\,\mathrm{Re}_d^{-0.68} \tag{67}$$

In the fully turbulent region, Azuma and Hoshino [74] found that a 1/7th power velocity distribution worked well. The skin friction coefficient there can be approximated as [44]

$$C_f = 0.073\left(\frac{r}{d\,\mathrm{Re}_d}\right)^{1/4} \tag{68}$$

and the film thickness may be estimated as

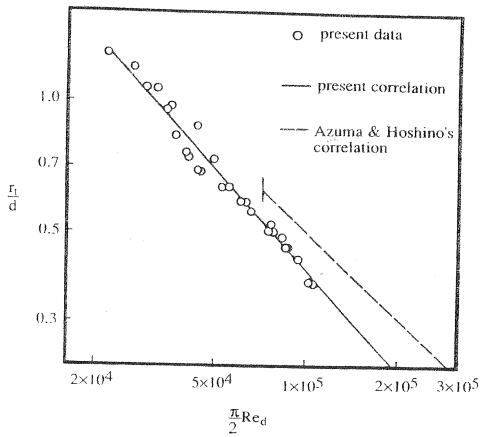

Figure 13 Location of turbulent transition for axisymmetric impinging jets (data from [44]).

$$\frac{h(r)}{d} = \frac{0.02091}{\mathrm{Re}_d^{1/4}}\left(\frac{r}{d}\right)^{5/4} + C\left(\frac{d}{r}\right) \tag{69}$$

with

$$C = 0.1713 + \frac{5.147}{\mathrm{Re}_d}\left(\frac{r}{d}\right) - \frac{0.02091}{\mathrm{Re}_d^{1/4}}\left(\frac{r}{d}\right)^{1/4} \tag{70}$$

5.2.2 Heat Transfer. Existing analytical solutions for heat transfer assume negligible heat transfer from the liquid surface; in particular, evaporation is neglected. This situation should prevail for a surface temperature, T_{sf}, that remains relatively low. If evaporation from the free surface becomes important, the theoretical expressions for the Nusselt number will underpredict.

Heat transfer in the downstream region has been modelled by Chaudhury [80], Nakaryakov et al. [45], Liu and Lienhard [79], Wang et al. [78], and Liu et al. [44]. Chaudhury used Watson's laminar velocity profiles to obtain similarity solutions for the liquid temperature field along a uniform temperature wall. Wang et al. developed solutions in the boundary layer region ($r < r_o$) that apply to arbitrary distributions of wall temperature and heat flux. Nakaryakov et al. [45] provide theoretical and experimental mass transfer results that are analogous to uniform wall temperature and very high Prandtl number. Their theory is based on a linear approximation to the velocity profile in the concentration boundary layer, which should be valid for the laminar regions of the flow when Pr >> 1.

Most experimental data for downstream heat transfer are for uniform wall heat flux, and this case has been modelled by Liu and Lienhard [79] and by Liu et al. [44] for both the laminar and turbulent regions of the flow. Liu and Lienhard separated the laminar flow into several thermal regions for Pr > 1:

Region 1. The stagnation zone.

Region 2. $\delta < h$ region: Neither the thermal nor viscous boundary layers reach the free surface; surface temperature and velocity, T_{sf} and u_m, are equal to the inlet temperature and velocity, T_f and u_f.

Region 3. $\delta < h$ and $\delta_t < h$ region: The viscous boundary layer has reached the free surface. The velocity outside the viscous boundary layer decreases with radius, but the surface temperature remains at the inlet temperature, T_f.

Region 4. $\delta < h$, $\delta_t = h$, and $T_w < T_{sat}$ region: In this region, the thermal boundary layer has reached the surface of the liquid sheet, and the temperature of the liquid surface increases with radius.

In the laminar regions, Liu and Lienhard applied the integral energy equation

$$\frac{d}{dr}\int_0^{\delta_t} ru\left(T - T_f\right)dy = \frac{q_w}{\rho c_p}r \tag{71}$$

where $T = T(r, y)$ is the liquid temperature profile. In the region before the thermal boundary layer reaches the free surface (region 2), they approximated the velocity profile as Eq. 61 and the temperature profile as

$$T(r,y) - T_w = (T_f - T_w)\left[\frac{3}{2}\frac{y}{\delta_t} - \frac{1}{2}\left(\frac{y}{\delta_t}\right)^3\right] \tag{72}$$

for T_w the wall temperature, which increases with radius. While $r < r_o$, the integral solution for the local heat transfer coefficient in the boundary layer region is approximately equal to

$$\mathrm{Nu}_d = 0.632\,\mathrm{Re}_d^{1/2}\,\mathrm{Pr}^{1/3}\left(\frac{d}{r}\right)^{1/2} \tag{73}$$

which shows the local heat transfer coefficient to decrease as $1/\sqrt{r}$.

Region 2 ends and region 3 begins where the viscous boundary layer reaches the film surface at r_o. In region 3, the integral solution is

$$\mathrm{Nu}_d = \frac{0.407\,\mathrm{Re}_d^{1/3}\,\mathrm{Pr}^{1/3}(d/r)^{2/3}}{\left[0.1713(d/r)^2 + (5.147r/\mathrm{Re}_d d)\right]^{2/3}\left[\frac{1}{2}(r/d)^2 + C_3\right]^{1/3}} \tag{74}$$

where†

$$C_3 = \frac{0.267(d/r_0)^{1/2}}{\left[0.1713(d/r_0)^2 + (5.147r_0/\mathrm{Re}_d d)\right]^2 \mathrm{Re}_d^{1/2}} - \frac{1}{2}\left(\frac{r_0}{d}\right)^2 \tag{75}$$

Region 3 ends and region 4 begins where the thermal boundary layer reaches the liquid surface at $r = r_1$; equations defining r_1 are given by Liu and Lienhard [79]. In region 4:

$$\mathrm{Nu}_d = \frac{0.25}{\frac{1}{\mathrm{Pr}\,\mathrm{Re}_d}\left[1 - (r_1/r)^2\right](r/d)^2 + 0.130\left[h(r)/d\right] + 0.0371\left[h(r_1)/d\right]} \tag{76}$$

where $h(r)$ is given by Eq. (64) above.

† Equation (75) is corrected for a typographical error which appeared in the *J. Heat Transfer*, Vol. 133, pp. 571–582, 1991 [44].

Region 4 will occur only for Pr less than a critical value near five;* otherwise, the thermal boundary layer does not grow fast enough to reach the surface of the liquid film, which thickens with increasing radius owing to viscous retardation. Liu et al. found that the predictions for regions 3 and 4 are within a few percent of each other, and they suggest that the prediction of region 3 be used for any Pr above unity. Regions 3 and 4 correspond to Watson's self-similar viscous flow regime.

Liu et al. estimated the fully turbulent heat transfer using the thermal law of the wall:

$$\mathrm{St} = \frac{q_w}{\rho c_p u_m (T_w - T_{sf})} = \frac{C_f/2}{1.07 + 12.7(\mathrm{Pr}^{2/3} - 1)\sqrt{C_f/2}} = f(C_f, \mathrm{Pr}) \tag{77}$$

From this, using Eqs. 68, 69, the Nusselt number may be obtained:

$$\mathrm{Nu}_d = \frac{q_w d}{k(T_w - T_f)} = \frac{8\,\mathrm{Re}_d\,\mathrm{Pr}\,f(C_f,\mathrm{Pr})}{49(h/d) + 28(r/d)^2 f(C_f,\mathrm{Pr})} \tag{78}$$

When Pr is well above unity, the equation may be simplified

$$\mathrm{Nu}_d = 0.0052\ \mathrm{Re}_d^{3/4}\left(\frac{d}{h}\right)\left(\frac{d}{r}\right)^{3/4}\left(\frac{\mathrm{Pr}}{1.07 + 12.7(\mathrm{Pr}^{2/3} - 1)\sqrt{C_f/2}}\right) \tag{79}$$

The theory for Prandtl numbers above unity is summarized in Table 5. Comparison of these equations to experimental data for a uniform profile laminar jet [44] is shown in Figure 14, and agreement is seen to be very good. Liu et al. also give integral solutions for Pr < 1.

* Liu and Lienhard [79] gave this value as 4.86. If the higher-order terms in the integral analysis are retained, the value becomes 5.23.

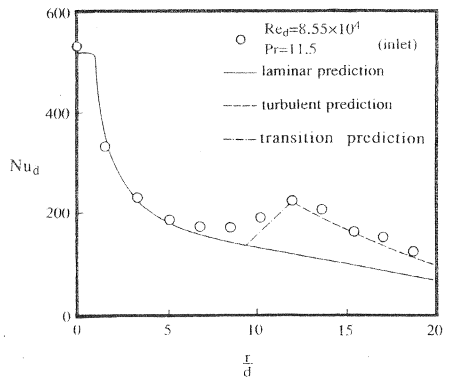

Figure 14 Comparison of laminar theory to data [44].

Table 5 Suggested Formulae for Local Nusselt Number of Laminar Jets with Pr > 0 (1)

Region	Range	Nu_d
Stagnation zone	$0 \le r/d < 0.787$	$0.745\ Re_d^{1/2}\ Pr^{1/3}$
Transition: stagn. to b.l.	$0.787 < r/d < 2.23$	$\left(\dfrac{\frac{27}{80} Re_d\ Pr \frac{r}{\delta}}{\frac{1}{2}\left(\frac{r}{d}\right)^2 - 0.2535} \right)^{1/3}$
Boundary layer region (2)	$2.23 < r/d < 0.1773\ Re_d^{1/3}$	$0.632\ Re_d^{1/2}\ Pr^{1/3} \left(\frac{d}{r}\right)^{1/2}$
Similarity region (3 and 4)	$0.1773\ Re_d^{1/3} < r/d < 1200\ Re_d^{-0.422}$	$0.407\ Re_d^{1/3}\ Pr^{1/3} \left(\frac{d}{r}\right)^{2/3} \left[\left[0.1713\left(\frac{d}{r}\right)^2 + \frac{5.147}{Re_d} \frac{r}{d}\right]^{2/3} \left[\frac{1}{2}\left(\frac{r}{d}\right)^2 + C_3\right]^{1/3} \right]$
	$(r_0/d < r/d < r_t/d)$	$C_3 = \left[\dfrac{0.267(d/r_0)^{1/2}}{\left[0.1713\left(\frac{d}{r_0}\right)^2 + \frac{5.147}{Re_d}\frac{r_0}{d}\right]} - \frac{1}{2}\left(\frac{r_0}{d}\right)^2 \right]$
Transition: laminar/turb.	1200	$Nu_{lam}(r_t) + \left[Nu_{turb}(r_t)\right] - Nu_{lam}(r_t) \dfrac{r - r_t}{r_h - r_t}$
Turbulent region	$r/d > 2.86 \times 10^4\ Re_d^{-0.68}$	$\dfrac{8\ Re_d\ Pr\ f(C_f, Pr)}{49(h/d) + 28(r/d)^2\ f(C_f, Pr)}$

5.2.3 Comments on the Accuracy of Laminar Axisymmetric Jet Theory. Although Liu et al. [44] found good agreement with the theoretical results, several cautions should be offered. First, their experiments made considerable efforts, to produce laminar jets and to keep the liquid cool enough to minimize evaporation or heat loss from the liquid surface. In practical situations, turbulence is likely to be present in the jet, and this will tend to raise the local Nusselt number downstream. If the liquid temperature rises too much over the radii of interest, evaporation may also occur, again increasing the Nusselt number.

Second, the theoretical solutions should be evaluated using liquid properties at the local liquid temperature (averaged across the liquid thickness). In particular, the liquid viscosity varies strongly with temperature for most liquids and may decrease significantly with radius. To use these results in calculating Nu_d and $T_w(r)$ a numerical integration in the radial direction is most expedient [79].

As an indication of the accuracy of these solutions when applied to nonideal situations, Womac et al. [81] compared area-average Nusselt numbers from the above results to measurements made beneath weakly turbulent jets. They found that the theory was low by 20% on average; however, the theory underpredicted by up to 80% for their largest and more turbulent nozzle.

Theory and data for turbulent circular jets are given Section 6.

5.3 Hydraulic Jumps

Jet impingement cooling systems sometimes operate with a hydraulic jump downstream of the region of impingement (Figure 1). The slow-moving liquid in the subcritical region presents degraded heat transfer characteristics [17], which make control of the jump location important in thermal design.

The open-channel hydraulic jump of undergraduate textbooks is usually manifested as a roiling turbulent free surface connecting the supercritical and subcritical regions of the flow. For planar flows of sufficient upstream depth, application of a one-dimensional momentum balance describes the relationship between upstream and downstream depth and velocity with an accuracy of about 1% over conditions ranging from laboratory flumes to hydroelectric power plants [82]:

$$\frac{s}{h} = \frac{1}{2}\left(\sqrt{1 + 8Fr_h^2} - 1\right) \tag{80}$$

where s is the depth downstream of the jump (subcritical flow) and $Fr_h = u_h / \sqrt{gh}$ is the supercritical Froude number based on upstream film thickness h and vertically averaged upstream speed, u_h. In such situations, the jump problem is both classical and well understood.

In contrast, Figure 1 shows a liquid surface that is fairly smooth, with a sharply defined and relatively steady hydraulic jump. In addition, the upstream (supercritical) liquid film is very thin, with a minimum thickness of about 100 μm for the 5-mm-diameter jet shown. Apart from these obvious differences in flow field, the

axisymmetric jump differs from the usual open-channel jump by the range of supercritical Froude numbers arising. For circular impinging jets, the upstream Froude number can be as much as several hundred, while typical open-channel flows have supercritical Froude numbers of no more than 20 or 30. Each of these factors contributes to unexpected deviations from the standard theory of the hydraulic jump.

Direct adaptation of the momentum-balance theory to axisymmetric impinging jet jumps was first made by Watson [69], and several subsequent investigators modified his theory slightly; the basic result is generally a prediction of the radial position of the jump. Watson's model consists primarily of calculating the radial variation of the supercritical Froude number, Fr_h, that results from the radial spreading and viscous drag on the thin upstream film.

Experimental tests of these models, however, have not been entirely satifactory. Watson himself presented data showing both good agreement and relatively poor agreement, and subsequent comparisons have been numerous: Olsson and Turkdogan [76], Ishigai et al. [17], Nakoryakov et al. [45], Bouhadef [83], Craik et al. [84], Errico [85], and Vasista [86] have each tested Watson's model. These studies did not systematically vary dimensionless groups, and most do not clearly distinguish an upstream Froude number. However, to focus on the trends of disagreement, the studies collectively show that Watson's model is less accurate when the downstream flow is too deep or when the upstream Froude number is too high.

One cause of the deviations is the velocity profile behind the jump. The experimental studies have shown that the flow just behind the jump can separate, creating a recirculating eddy attached to the wall. This separation is a result of the abrupt increase in hydrostatic pressure at the jump, an effect that is clearly worsened when the downstream flow is deeper. The complex flow field behind the jump has a serious effect on any one-dimensional momentum-conservation model.

A second complication is that the shape of the jump surface has been observed to have several forms, variously being smooth, being curved, showing standing or radiating waves, and showing outright instability. The parameters reported to be responsible for these changes include increasing downstream depth [84], increasing volume flow [85, 87], and increasing upstream Froude number [17]. Typically, the changes reported are described as some form of instability in the smooth free surface of Figure 1. These variations in the jump surface have a controlling influence on the velocity profile beyond the jump and affect the breakdown of the jump radius predictions.

Liu and Lienhard [70] examined these trends in detail. They concluded that the stability of the jump's free surface is primarily dependent on the liquid surface tension, which can play a significant role only when the subcritical fluid layer is relatively thin. The thinness of the downstream flow is a condition that has seldom been met in planar jump experiments, but which is a regular feature of axisymmetric hydraulic jumps. In addition, their data show that the large supercritical Froude number (or equivalently the large ratio of downstream to upstream depth) is the other key factor in the failure of standard jump theory as applied to the circular jump. Both observations show that the thinness of the upstream and downstream films, rather

than axisymmetry per se, is responsible for the failure of one-dimensional theories of the jump. This conclusion was corraborated by an experiment on a thin planar film.

Liu and Lienhard characterized the balance between the hydrostatic pressure force behind the jump and the surface tension force along the surface of the jump using a jump Weber number:

$$\mathrm{We} = s\sqrt{\frac{\rho g}{\sigma}} \tag{81}$$

where s is the downstream [subcritical] depth of the liquid film and σ is the surface tension. By comparing We to observations of the jump's surface shape, Liu and Lienhard found that the shape was indeed influenced by the Weber number, with the most stable interfaces occurring for We below about 2 and instability occurring for We above 5 to 6.

A full prediction of the circular jump radius will depend on six dimensionless groups. If the initial conditions are set at the jet nozzle, an appropriate functional equation is

$$\frac{r_j}{d} = F\left(\mathrm{Re}_d, \mathrm{Fr}_d, \mathrm{We}, \frac{s}{d}, \frac{r_s}{d}\right) \tag{82}$$

Here, the dimensionless jump radius, r_j/d, is a function of: the jet Reynolds and Froude numbers, $\mathrm{Re}_d = u_f d/\nu$ and $\mathrm{Fr}_d = u_f/\sqrt{gd}$, which together describe the radial evolution of the local supercritical Froude number; the jump Weber number, which controls the jump shape; and the dimensionless downstream depth, s/d, and the dimensionless radius, r_s/d, at which that depth occurs. No complete theory is currently available for predicting r_j, although a substantial amount of data for r_j can be found in the paper by Liu and Lienhard.

Numerical models for the related problem of hydraulic jumps in a thick radial film have been given by Faghri and co-workers [88–90].

5.3.1 Suppressing Hydraulic Jumps. A thermal designer is probably most interested in preventing a hydraulic jump and its associated decrease in h. Several comments can be made.

First, the jump results from poor downstream drainage of the liquid or from downstream obstruction of the liquid sheet. It can be inhibited by ensuring that liquid flows easily off of the target surface. At low speeds or small jet diameters, a jump can occur on a flat surface that appears to have no obstruction to drainage downstream, simply as a result of the wall drag on the liquid layer; in this case, the jump can be removed by reducing the target radius.

Second, the jump can always be moved downstream by increasing the jet's velocity, Reynolds number, or Froude number.

Third, hydraulic jumps represent a conversion of liquid momentum to hydrostatic pressure thrust that can only occur when the jet impacts vertically downward onto the target; a very different, dripping phenomenon occurs when the jet impacts vertically upward onto a target [79].

Lastly, it should be mentioned that boiling within the supercritical film may act as a flow obstruction that promotes a hydraulic jump.

6 TURBULENT AND SPLATTERING AXISYMMETRIC JETS

This section describes heat transfer by axisymmetric, turbulent jets and the processes of liquid splattering that may occur during turbulent jet impingement. This section deals with only processes downstream of the stagnation zone, which was addressed in detail in Sections 4.4 to 4.7.

Turbulence in an axisymmetric jet is carried into the radially spreading liquid film, where it has two primary effects. First, the turbulence tends to increase convective heat transfer in the boundary layer downstream of the stagnation zone and tends to promote turbulent transition of the thin liquid sheet. The turbulent sheet has greater skin friction than a laminar sheet: Measurements of nonsplattering turbulent jets [13] show that the liquid surface speed begins to drop at $r \approx 2.5\ d$, sooner than predicted by laminar flow theory.

The second effect of jet turbulence is to disturb the surface of the incoming jet. These disturbances are carried into the thinning liquid sheet, where the radial spreading can produce a strong increase in their amplitude. If the initial disturbances are large enough, the amplified disturbances can cause droplets to break free from the liquid sheet, resulting in splattering (Figure 15).

Splattering is more important when the jets are longer and have a higher Weber number, because the disturbances reaching the sheet are then larger. Strong splattering can result in atomization of 30 to 70% of the incoming liquid, and because the airborne droplets no longer contribute to cooling the wall, heat transfer far downstream is degraded. On the other hand, splattering has no independent influence on heat transfer in

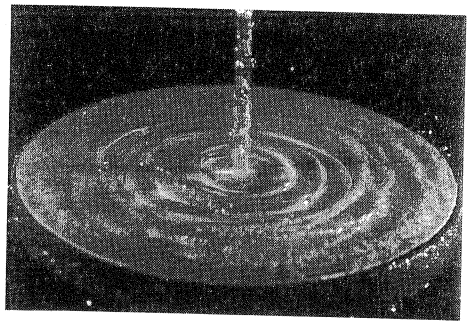

Figure 15 Splattering turbulent jet showing radially travelling waves: $Re_d = 28000$, $\xi = 0.11$, $\omega = 4550$, fully developed tube nozzle.

the stagnation region, because the droplets break away several diameters downstream of it. Stagnation-zone heat transfer can be predicted using the results given in Section 4.5.

Splattering occurs in isothermal situations, as well as those with heat transfer, and its ramifications extend beyond thermal problems. In cleanroom situations, where impinging jets may be used for post-etching debris removal, splattered liquid can produce airborne contaminants. In metal-jet spray-forming operations, splattering is a primary cause of reduced yield. In situations involving toxic chemicals, splattered droplets can create a hazardous aerosol whose containment necessitates potentially costly air filtration.

6.1 Splattering

6.1.1 The Mechanics of Splattering. Initial studies of splattering by Errico [85] and by Lienhard et al. [91] demonstrated that it is driven by the disturbances on the surface of the impinging jet. Thus, undisturbed laminar jets do not splatter, unless they are long enough to have significant capillary instability. Turbulent jets, on the other hand, develop surface roughness as a result of liquid-side turbulent pressure fluctuations, and they are highly susceptible to splattering.

Errico [85] induced splattering for laminar jets by creating surface disturbances with a fluctuating electric field. His results showed that splattering commenced at progressively lower jet velocities when the amplitude of disturbance was increased and that splattering occurred as the disturbances from the jet spread radially on the liquid film. When a turbulent jet strikes a target, similar travelling waves originate near the impingement point and travel outward on the film (see Figure 15). When the jet disturbances are sufficiently large, these waves sharpen and break into droplets. All observations indicate that the amplitude of the disturbances on the jet governs splattering. They further indicate that splattering is a non-linear instability phenomenon, because the liquid film is clearly stable to small disturbances but unstable to large ones [92].

Varela [93] developed an analytical model of finite-amplitude disturbance evolution on an inviscid axisymmetric liquid sheet. (The inviscid approximation is justified in the region before the boundary reaches the liquid surface.) Varela applied a multiple-scale analysis to the water-wave equations, obtaining a variable coefficient Korteweg-deVries equation that describes the modulation of radially travelling disturbances which originate on the incoming jet. Numerical integration of these equations by Dr. Peter Schmid showed that the initial disturbances evolve into a train of sharp solitary waves (Figure 17). Moreover, the sharpening of the waves depends on their initial amplitude, and those of sufficiently large amplitude exhibit behavior suggestive of wavebreaking.

Once droplets break away from the liquid sheet, they remain airborne. Lienhard et al. [91] made phase-doppler measurements of the size and speed of the departing droplets and found that the droplets travel at a low angle with nearly the speed of the incoming jet; thus, they do not fall back into the liquid film at an appreciable rate. Their measurements, and stroboscopic observations by Errico [85], show that drop-

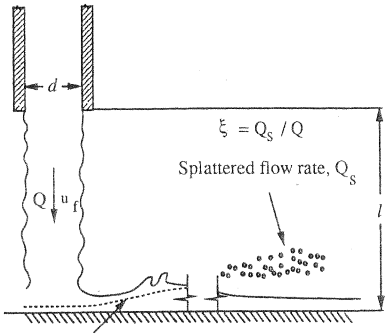

Figure 16 Schematic drawing of the splattering process.

lets leave the liquid sheet within a fairly narrow radial band, beyond which no further splattering occurs. The radius of departure was estimated to be $r/d \approx 4.5$.

6.1.2 The Fraction of Liquid Splattered. Measurements of the splattered liquid flow rate for fully turbulent turbulent jets were first reported by Lienhard et al. [91] in the form of the ratio of splattered flow rate, Q_s, to the incoming flow rate, Q (Figure 16):

$$\xi = \frac{Q_s}{Q} \tag{83}$$

This quantity is easily measured by capturing the unsplattered liquid and determining its flow rate. Lienhard et al. also proposed a model for splattering that related the rms

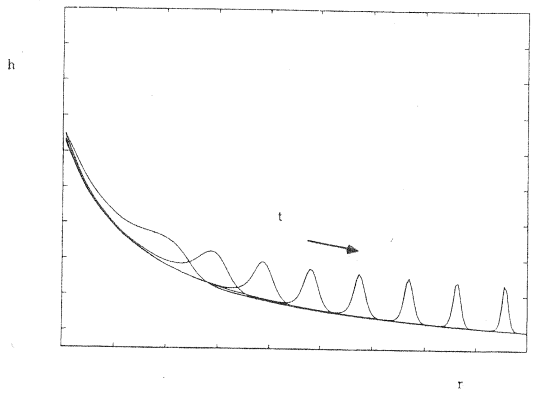

Figure 17 Time evolution of a solitary wave travelling along an inviscid axisymmetric sheet [92,93].

amplitude of jet surface disturbances to the rate of splattering, as ξ should be greater for larger disturbance amplitudes. In this model, turbulent pressure fluctuations in the jet cause the initial surface disturbances on the jet, which are then assumed to evolve by Rayleigh's capillary instability [94] as the jet travels to the target.* The model's prediction of the rms amplitude of disturbances reaching the target scales with a parameter, ω:

$$\omega = \mathrm{We}_d \exp\left(\frac{0.971}{\sqrt{\mathrm{We}_d}}\frac{l}{d}\right) \tag{84}$$

Here,

$$\mathrm{We}_d = \rho u_f^2 d/\sigma \tag{85}$$

is the jet Weber number, and l is the nozzle-to-target separation.

Lienhard et al. observed good correlation of ξ with ω. Their result was refined by Bhunia and Lienhard [95], who gave the following curve-fit (Figure 18):

$$\xi = -0.258 + 7.85\times10^{-5}\omega - 2.51\times10^{-9}\omega^2 \tag{86}$$

This result applies for $4400 < \omega < 10{,}000$. The lower limit on ω is chosen to ensure that the predicted ξ is at least 4%; below this level there is considerable scatter and high uncertainty in the measurements. The ω scaling parameter is valid for $10^3 < \mathrm{We}_d < 5 \times 10^3$ and $l/d < 50$.

For larger l/d or We_d the ω model fails. Instead, l/d and We_d must be treated as independent variables. In Figure 19, the amount of splattering, ξ, is shown as a function of nozzle-to-target separation, l/d, for several nozzle diameters and Reynolds numbers [95]. Each solid line represents data for a narrow range of Weber numbers, varying by less than ±3% around the stated mean value, a range equal to the experimental uncertainty of We_d. As the figure shows, for constant We_d, ξ is a function of l/d; different curves are obtained for different Weber numbers, with splattering increasing as the Weber number increases.

To study the effect of surface tension directly, a solution of approximately 10% by volume of isopropanol in water was used, having $\sigma = 0.042$ N/m (vs. 0.072 N/m for pure water). These data show good agreement with data for water when scaled with the Weber number (Figure 20). Splattering increases as surface tension decreases.

At any given Weber number and nozzle-target separation, the splatter fraction, ξ, depends extremely weakly on the Reynolds number, if at all. For example, in the data

* This particular assumption is open to question, as the spectral data presented below will show. In particular, the turbulent pressure fluctuations driving instability cover a broad range of short wavelengths ($\lambda < d$), the most energetic of which should be *stable* according to Rayleigh's results.

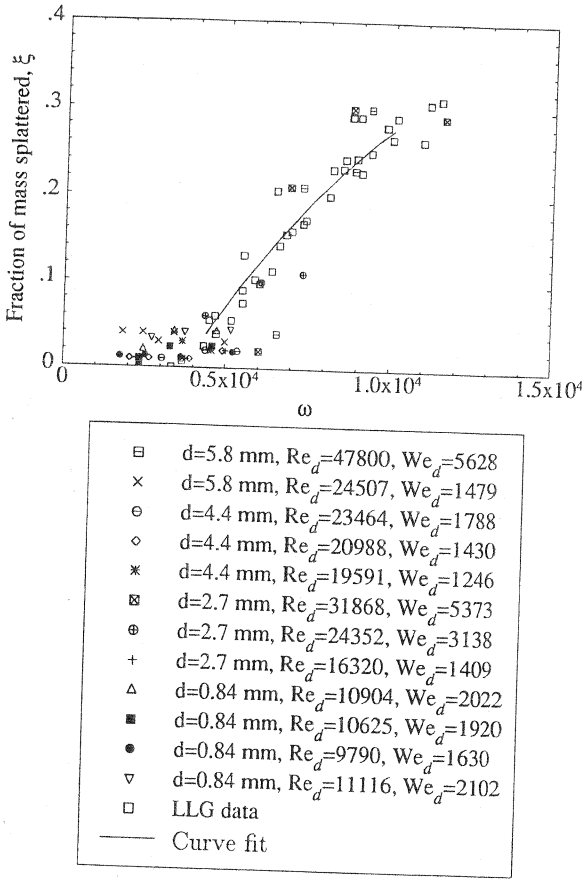

Figure 18 Omega scaling of the splattered fraction [95].

set for We_d = 5500, the Reynolds number increases by a factor of 1.5 without any discernible change in the splatter fraction, ξ. In contrast, a factor of 1.3 increase in the Weber number (from 5500 to 7300) produces significant increase in the splatter fraction (roughly +25%).

An influence of Reynolds number would be expected to arise primarily from viscous effects near solid boundaries, either in setting the pipe turbulence intensity or as an influence of the viscous boundary layer along the target. The stagnation-point boundary layer is extremely thin relative to the liquid layer, and thus it may have little effect on the surface waves near the region of impingement. The pipe-turbulence variation maybe quantified by observing that the ratio of rms turbulent speed to friction velocity, u'/u_*, is nearly independent of Reynolds number in fully developed turbulent pipe-flows [95]. Therefore, after using the definition,

$u_* = u_f\sqrt{f/8}$, and the Blasius friction factor equation ($f = .316\ \mathrm{Re}_d^{-1/4}$ for $4000 < \mathrm{Re}_d < 10^5$), one finds

$$\frac{u'}{u_f} \propto \frac{u_*}{u_f} \propto \sqrt{f} \propto \mathrm{Re}_d^{-1/8}$$

This weak dependence of the turbulence intensity on the Reynolds number may explain the lack of any significant dependence of splattering on Re_d.

6.1.3 The Relation of Splattering to Jet Surface Disturbances. Referring to Figures 19 and 20, we see that very little splattering occurs close to the jet exit (small

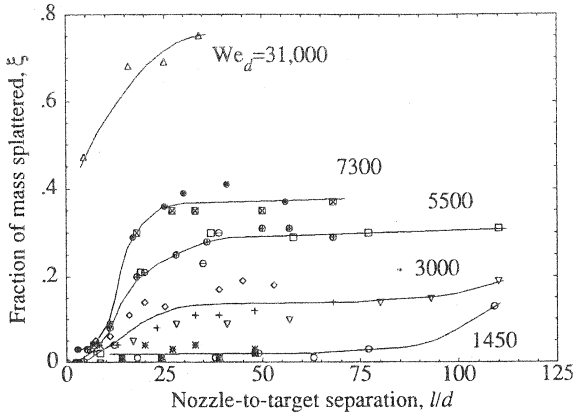

d=4.4 mm, Re_d=98097, We_d=31243
d=4.4 mm, Re_d=48284, We_d=7564
d=2.7 mm, Re_d=37141, We_d=7096
d=5.8 mm, Re_d=47800, We_d=5628
d=4.4 mm, Re_d=41437, We_d=5420
d=2.7 mm, Re_d=31868, We_d=5373
d=5.8 mm, Re_d=35986, We_d=3101
d=4.4 mm, Re_d=30090, We_d=2858
d=2.7 mm, Re_d=24580, We_d=3108
d=5.8 mm, Re_d=24507, We_d=1479
d=4.4 mm, Re_d=20988, We_d=1430
d=2.7 mm, Re_d=16320, We_d=1409

Figure 19 Splattering as a function l/d and We_d [95].

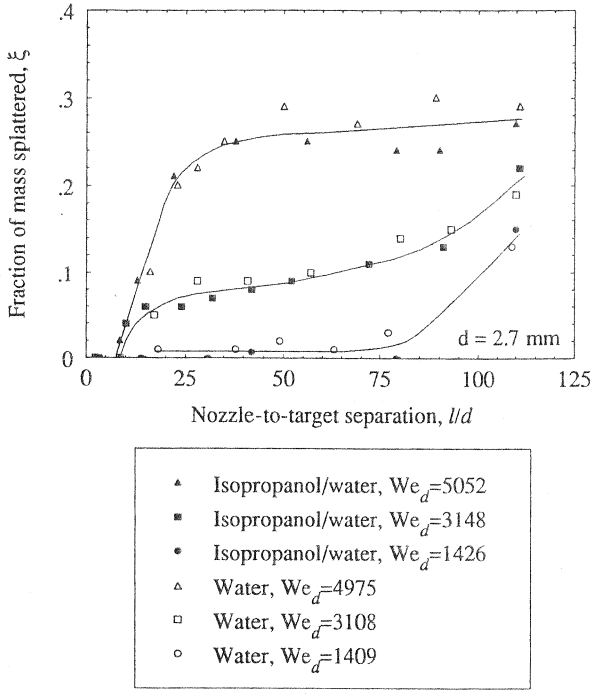

Figure 20 Splattering as a function l/d and We_d for liquids of different surface tension [95].

l/d), typically less than 5%. Beyond this region, the amount of splattering at first increases with distance, l/d. Farther downstream, it reaches a plateau. To explain these observations we may refer to direct measurements of the amplitude of turbulent liquid jet surface disturbances.

Bhunia and Lienhard [96] used a laser-sheet and high frequency-response photodiode to measure the instantaneous diameter of turbulent liquid jets. They obtained the rms amplitude of jet surface disturbances, δ_{rms}, at different axial locations along jets of various Weber numbers (Figure 21ab). Starting from nearly zero near the nozzle exit, δ_{rms} initially grows rapidly as the jet moves downstream; farther downstream the growth rate diminishes and the rms disturbance tends to an asymptotic limit. The dependence of δ_{rms}/d on jet Weber number is also apparent.

This growth of disturbances is the probable cause of the increase in the splatter fraction as the nozzle-to-target separation is increased. The steadily decreasing rate of amplitude growth results in a plateau of the disturbance amplitude that corresponds to the plateau in the splatter fraction data.

Direct comparison of the measurements of δ_{rms} to data for ξ and shows a reasonable correlation between the size of δ_{rms}, and the fraction of liquid splattered (Figure 22). This graph was obtained by plotting previously measured splatter fraction ξ

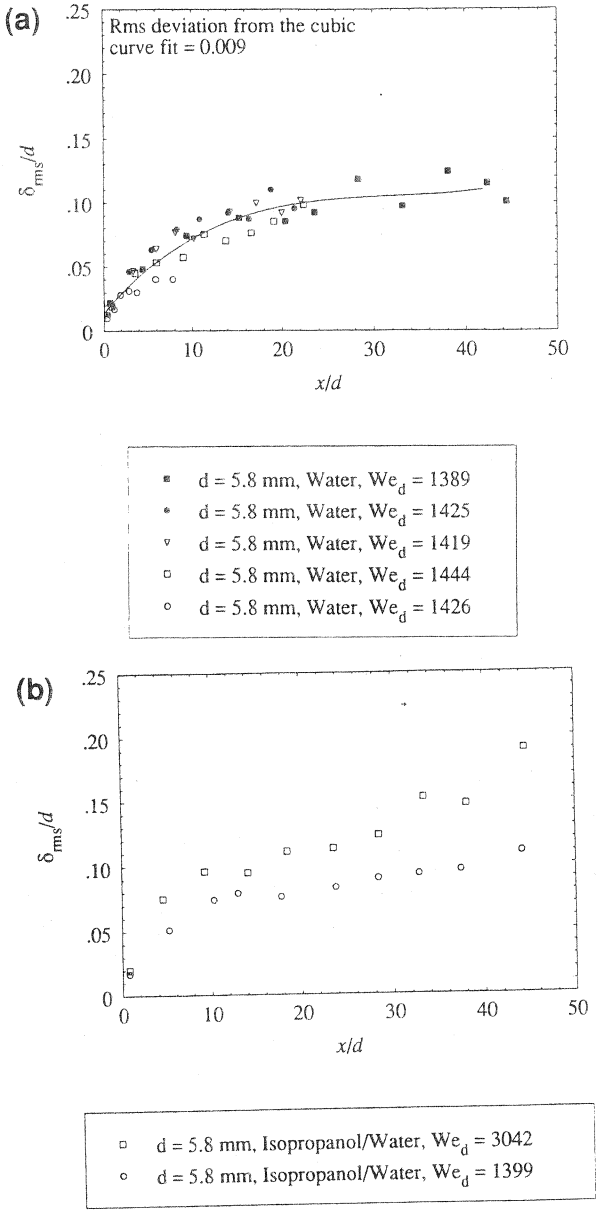

Figure 21 Root-mean-square surface roughness data: (a) several runs at fixed Weber number, showing variability of data; (b) comparison of roughnesses at two different Weber numbers [96].

values against δ_{rms}/d for jets of the same Weber number and $l/d = x/d$ [96]. Each set of data for a given nozzle diameter and jet Weber number consists of measurements at several different axial locations, x/d. The correlation is reasonably clear, given that both ξ and δ_{rms} have significant variability, and it provides further evidence that splattering is due to surface disturbances on the jets and is governed by the amplitudes of those disturbances.

For very long, low Weber number jets the plateau of splattering ends, and ξ again increases with l/d (Figure 20). This may reflect the appearance of ordinary capillary instability on these jets. Specifically, when the Weber number is low, the asymptotic turbulence-generated surface roughness is small compared with the jet radius. Thus, the still nearly cylindrical jet can give up surface energy by the usual Rayleigh-type instability. In contrast, at higher Weber numbers, the turbulent disturbances grow to be as large as the jet radius, effectively breaking up the jet.

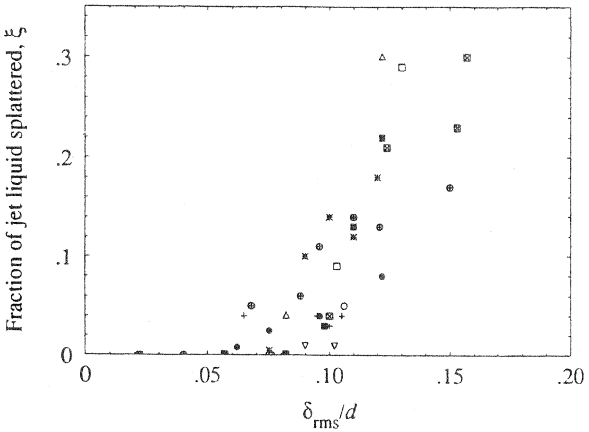

Figure 22 Splatter fraction as a function of rms surface roughness [96].

6.1.4 The Onset of Splattering. Some problems arise in defining the onset point of splattering. Because the process of splattering involves turbulent flow, sporadic splattering of droplets occurs at much lower jet velocities than those that would cause any significant amount of sustained splattering (other parameters remaining the same). Consequently, the onset point is more accurately definable in terms of a non-zero level of splattering. Bhunia and Lienhard [95] defined the onset of splattering as the point where 5% of the incoming fluid is splattered. Because the amount of splattering at a fixed l/d depends strongly on the jet Weber number and not on the Reynolds number, the onset point is uniquely identifiable by its l/d and We_d. In other words, for a jet of a given Weber number, the onset point is reached at a certain l/d.

Figure 23 shows the data for onset points. A correlation for the onset point data is

$$\frac{l_o}{d} = \frac{130}{1+5\times10^{-7}\,\mathrm{We}_d^2} \tag{87}$$

This correlation supercedes the result of Lienhard et al. [91], who reported $\omega \geq 2120$ for the appearance of *any* splattering; within the range of validity of ω scaling, 5% splattering corresponds to ω between 4100 and 5100.

For low Weber numbers, near 100, turbulent disturbances are strongly damped by surface tension, and the observed onset lengths are actually rather close to the capillary breakup lengths. In this range, splattering is essentially of drop impingement type.

In this connection, it should be noted that the relative importance of turbulence and surface tension is characterized by a balance of rms turbulent dynamic pressure and capillary pressure. Thus, the appropriate Weber number for characterizing the splattering mechanism is based on the rms fluctuating component of the velocity, u', and the rms height of the surface disturbances, δ_{rms}:

$$\hat{\mathrm{We}} = \frac{\text{turbulent dynamic pressure}}{\text{capillary pressure}} = \frac{\rho u'^2}{\sigma/\delta_{rms}} = \frac{\rho u'^2 \delta_{rms}}{\sigma} \tag{88}$$

$\hat{\mathrm{We}}$ should be $\mathcal{O}(1)$ or greater when turbulence drives splattering. However, u' and δ_{rms} are not easily available, while u_f and d are, so we have used

$$\mathrm{We}_d = \frac{\rho u_f^2 d}{\sigma} = \hat{\mathrm{We}} \Big/ \left[\frac{\delta_{rms}}{d}\left(\frac{u'}{u_f}\right)^2\right] >> 1 \tag{89}$$

which is 100 to 1000 times larger than the Weber number, $\hat{\mathrm{We}}$, that actually characterizes physical processes involved here (u'/u_f is a few percent in magnitude and $\delta_{rms}/d < 0.5$).

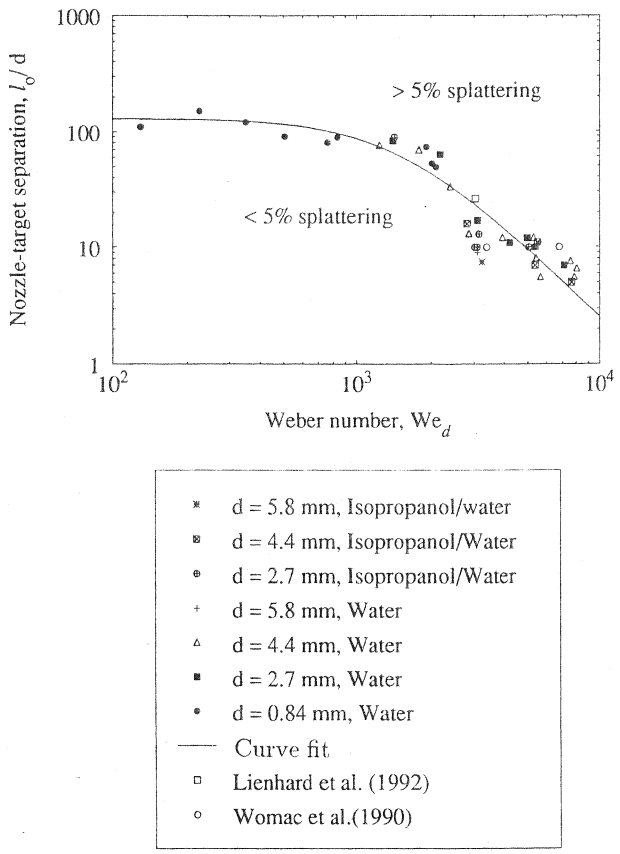

Figure 23 Onset of splattering [95].

6.1.5 The Influence of Surfactants on Splattering. Surfactants lower surface tension by forming a surface-adsorbed monolayer at the liquid surface. When a new liquid surface is formed, some time is required for surfactant molecules to diffuse to the surface in sufficient concentration to alter the surface tension. To study the role of surfactants in splattering, Bhunia and Lienhard [95] used a mixture of approximately 0.2% detergent in water. This reduced the surface tension of the static solution (liquid surface at rest) to 0.027 N/m and corresponded to a saturated concentration of surfactant. They found that the presence of the surfactant did not alter the amount of splattering. The splatter fraction for the surfactant-laden jet is identical to that for a pure-water jet of the same velocity, diameter, and length; in fact, if the surfactant-jet Weber number is calculated on the basis of pure-water surface tension, the curves for the surfactant jets are identical to those of the pure jets. From the standpoint of

splattering, the surface tension of the surfactant jet is effectively the surface tension of the pure liquid.

To further explore this behavior, Bhunia and Lienhard [96] measured the surface-roughness evolution of jets containing surfactant. They found that the surface roughness of a surfactant-laden jet evolved at the same rate as for a pure-water jet of the same size and speed. In other words, surfactants do not decrease the stability of the turbulent jet surface under conditions like these.

A possible cause of this behavior is the finite time required to establish a saturated concentration of surfactant on the jet surface. Inside the nozzle, the surfactant is in the bulk of the liquid. When the liquid exits the nozzle, a new free surface is formed that is not initially saturated with surfactant. During the time needed for the surfactant to diffuse from the bulk to the free surface, the surface remains unsaturated, and in this initial length of the jet, the surface tension remains near that of pure water. Turbulent free-surface renewal may also tend to limit the surface concentration of surfactant, if the surface layer of surfactant is continuously being reentrained into the bulk liquid.

6.1.6 Power Spectra of Surface Disturbances. Figure 24 shows wavenumber spectra of jet-surface disturbances at several different axial locations. The ordinate is proportional to the power spectrum of the free surface disturbance amplitude, $G(k_1 l)$ (see Eq. 92 below), and the abscissa is uk_1, where k_1, is the wavenumber in the direction of the jet axis, u is the free surface velocity, and l is the integral scale of turbulence.

These graphs of power spectrum vs. disturbance wavenumber show that broad-band turbulent disturbances dominate over any single wavenumber disturbance related to a Rayleigh-type instability. In addition, these log-log spectral plots show a portion of very nearly linear decrease in the spectral amplitude, characteristic of high wavenumber turbulence. Except for measurement locations very near the nozzle, the slope of this linear portion is –19/3, so that the spectra decay as $k_1^{-19/3}$.

A model that explains the spectral decay was constructed by Bhunia and Lienhard [96], who approximated the jet surface as planar. The liquid pressure fluctuations near the free surface are balanced by the surface tension, so that along the plane of the surface

$$p = -\sigma\left(\frac{\partial^2\delta}{\partial x^2} + \frac{\partial^2\delta}{\partial y^2}\right) \tag{90}$$

Bhunia and Lienhard modelled the liquid-side pressure fluctuations as those of a spatially homogeneous turbulence. By treating both p and δ as stationary random functions, they obtained the following equation for the mean-squared amplitude of surface disturbances:

$$\overline{\delta^2} = \int_{-\infty}^{\infty}\int_{-\infty}^{\infty} \frac{1}{\sigma^2\left(k_1^2 + k_2^2\right)^2} \int_{-\infty}^{\infty} F(k)\,dk_3\,dk_2\,dk_1 \tag{91}$$

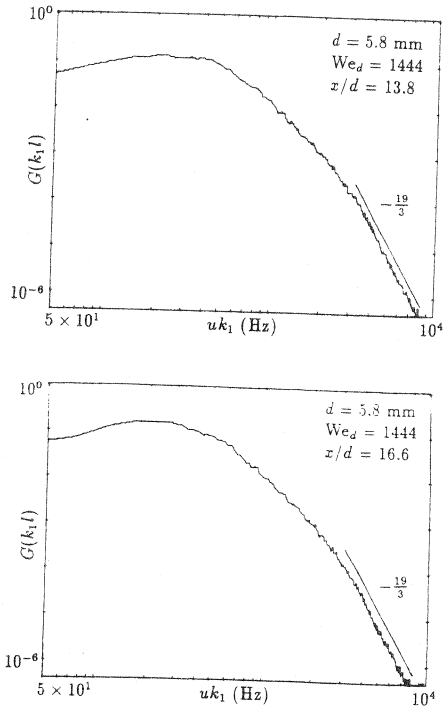

Figure 24 Measured power spectra of turbulent liquid-jet surface disturbances. Ordinate is proportional to $G(k_1 l)$ [96].

Here, $F(k)$ is the turbulent pressure spectrum, and (k_1,k_2,k_3) are the (x,y,z) components of a wavevector of magnitude k. For isotropic, homogeneous turbulence [97],

$$F(k) \sim 0.26 \rho^2 u'^4 l^3 (kl)^{-13/3}, \quad kl >> 1$$

where u' is the rms turbulent velocity and l is the integral scale of turbulence.

To relate these results to the measured one-dimensional spectrum of the surface disturbances, $G(\eta)$, they introduced the definition

$$\frac{\overline{\delta^2}}{l^2} = \int_0^\infty G(\eta) d\eta \tag{92}$$

where η is the wavenumber of the free surface disturbances nondimensionalized with the integral scale of turbulence, l. From Eqs. 91 and 92, it follows that at high wavenumbers ($\eta >> 1$) the disturbance spectrum is

$$G(\eta) \sim 0.26 \times 2\pi \frac{\rho^2 u'^4}{\sigma^2} \frac{l^{-13/3}}{k_p^3} \int_{-\infty}^{\infty} \frac{dk_3}{\left(k_p^2 + k_3^2\right)^{13/6}} \tag{93}$$

where we have transformed from Cartesian to polar coordinates in the wavenumber plane, $(k_1,k_2) \rightarrow (k_p,\theta)$, with $\eta = k_p l$ and $k_p = \sqrt{k_1^2 + k_2^2}$. After evaluating the integral, the one-dimensional spectrum of free surface turbulent disturbances (measured along any direction θ) is found to be

$$G(\eta) \sim 2.41 \left(\frac{\rho^2 u'^4 l^2}{\sigma^2} \right) \eta^{-19/3}, \quad \eta >> 1 \tag{94}$$

This analysis explains the observed –19/3 slope in the log-log plots of the disturbance spectra as a consequence of the $k_1^{-7/3}$ variation of the one-dimensional spectrum of the pressure fluctuations and a factor of k_1^{-4} introduced by the derivatives of δ in the capillary force balance equation.

6.2 Turbulent Axisymmetric Jet Heat Transfer

Turbulent jets usually create greater heat transfer coefficients than otherwise identical laminar jets. Turbulent heat transfer in the stagnation zone was discussed at length in Sections 4.4 to 4.7. Downstream of the stagnation region, the heat transfer coefficient decreases with increasing radius. The decrease is fairly rapid for small radii (roughly $1 < r/d < 2$) as the flow leaves the stagnation zone and the boundary layers thicken. Both splattering and nonsplattering jets show a flattening or a slight increase in local h in the vicinity of $r/d = 3 - 5$; this increase is generally attributed to a full turbulent transition of liquid film. Thereafter, the local heat transfer coefficient decreases with radius in a fashion described by the turbulent law-of-the-wall.

Data for nonsplattering, turbulent jets were obtained by Stevens and Webb [61] in the range $r/d < 7.5$ and $6800 < Re_d < 42200$. Data including splattering were obtained by Lienhard et al. [91] for $19000 < Re_d < 69000$ and $r/d < 28$. Both studies used fully developed turbulent water jets. Stevens and Webb provide a correlating equation for the region upstream of the turbulent transition radius, which they observed to shift with Reynolds number; the coefficients of this equation were found to vary with nozzle size.

Lienhard et al. [91] constructed a model for the downstream variation of the heat transfer coefficient that accounted for the occurrence of splattering. This model assumes that the radius of droplet departure coincides with the location of turbulent transition, both occurring at $r/d = 4.5$. In the boundary layer region between the stagnation zone and $r/d = 4.5$, they correlated the ratio of average turbulent h to average laminar h as a function of the ω parameter (Figure 25). The enhancement of heat transfer in this region is due to the very strong wave-like disturbances on the thin liquid film and can amount to as much as a factor of 3.

Splattering of droplets removes both mass and momentum from the liquid sheet. Lienhard et al. coupled conservation of mass and momentum with their correlation for the splattered mass, ξ, to obtain estimates for the initial velocity and thickness

of the turbulent liquid sheet after splattering ($r/d > 4.5$). They then applied a skin friction equation and the thermal law-of-the-wall to estimate the local Nusselt number downstream.

Their prediction is compared to that for a laminar incoming jet in Figure 26 for various values of the splatter fraction ξ and fixed Reynolds and Prandtl numbers. Raising the fraction of liquid splattered causes increasing deterioration of the heat transfer far downstream; however, in most cases for r/d less than about 20, the turbulent jet heat transfer is still well above that for a laminar jet.

These results can be combined to find the radial variation of local h for turbulent splattering jets. The stagnation zone Nu_d can be calculated from equations given in Section 4.5, Nu_d between the stagnation zone and $r/d = 4.5$ can be found from the laminar equations (Section 5.2) and Figure 25, and the heat transfer farther downstream can be obtained from the equations in Lienhard et al. [91]. The combined prediction is compared to data in Figure 27; the overall agreement is good.

7 OTHER ASPECTS OF JET IMPINGEMENT

7.1 Average Heat Transfer Coefficients

Several studies have correlated average heat transfer coefficients for axisymmetric impinging jets. In Sections 5 and 6, these jets were shown to have a strong variation in local h as the radial distance from the stagnation point increases. Thus, the average

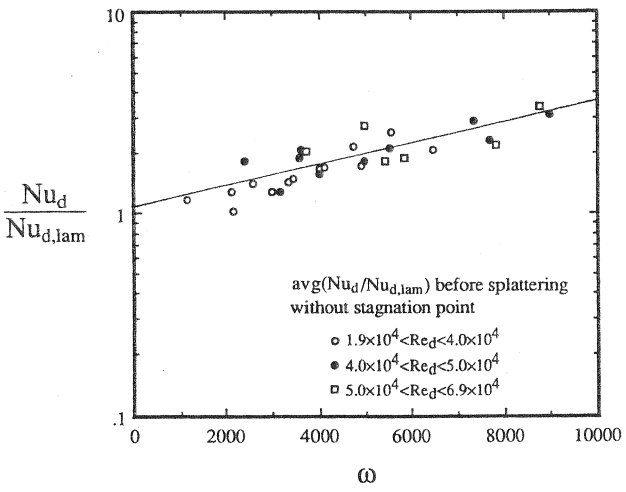

Figure 25 Augmentation of average Nu_d relative to laminar flow in the boundary layer region upstream of the splattering radius, $r/d = 4.5$ [91].

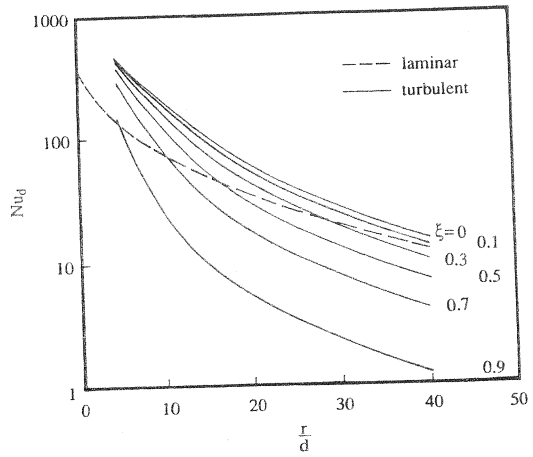

Figure 26 Estimated local Nusselt number for the region after splattering: $Re_d = 50{,}000$; Pr = 10 [91].

heat transfer coefficient, $\bar{h}$, depends strongly on the ratio of jet diameter, d, to the target diameter, D, over which the average is taken. Changes in nozzle conditions — velocity profile or turbulence levels — will also affect the average h strongly, especially when the target area is not much larger than the jet. In addition, increases in the liquid bulk temperature with radius can cause introduce variable properties effects into correlations for $\bar{h}$.

Metzger et al. [98], for example, correlated the average Stanton number for isothermal surfaces as a product of powers of Re_d, Pr, and D/d:

$$St = \frac{\bar{h}}{\rho c_p u_f} = 2.74\, Re_d^{-0.652}\, Pr^{-0.513} \left(\frac{D}{d}\right)^{-0.774} \left(\frac{\mu_0}{\mu_{aw}}\right)^{-0.37} \tag{95}$$

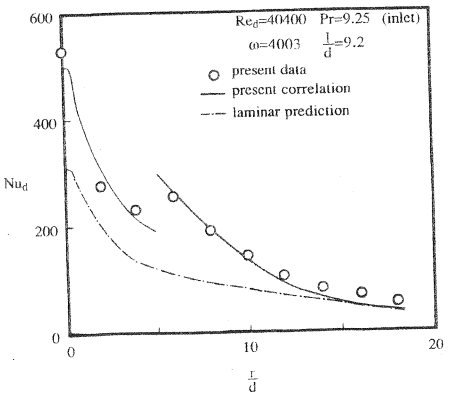

Figure 27 Comparison of local Nu_d data for turbulent jets to the model of Lienhard et al. [91].

This correlation is based on various data for fully turbulent tube nozzles within the ranges $2200 \le \mathrm{Re}_d \le 138200$, $3.0 \le \mathrm{Pr} \le 151$, $1.75 \le D/d \le 13.2$, and $0.6 \le \mu_0/\mu_{aw} \le 1.0$. Here, μ_0 is evaluated at the wall temperature, and μ_{aw} is evaluated at the adiabatic wall temperature, which is usually almost equal to the jet temperature. The correlation is accurate to about 25% in this range of parameters.

Steven and Webb [61] developed a fairly complicated algebraic equation that correlated the integral of their local h measurements for D/d less than about 8 to an accuracy of ±15. These results were obtained for fully turbulent water jets striking a uniform heat flux surface with $6800 \le \mathrm{Re}_d \le 41000$.

Womac et al. [99] measured $\bar{h}$ for small diameter jets of FC-77, with an eye toward electronics cooling applications. Their results also suggest that $\bar{h}$ can be greater for single *submerged* jets than for single unsubmerged jets in some cases, because, at large radii, the unsubmerged jet's liquid film increases in temperature and decreases in speed, whereas the submerged jet mixes vigorously with colder surrounding fluid.

Womac et al. [81] have examined in detail the problem of constructing correlations for average heat transfer coefficients. While their specific interest is in electronics cooling applications, they also considered the results mentioned above. On that basis, they proposed the following correlation that separately weighs the stagnation-zone and downstream contributions to $\bar{h}$:

$$\frac{\overline{\mathrm{Nu}_d}}{\mathrm{Pr}^{0.4}} = 0.516\,\mathrm{Re}_d^{0.5}\left(\frac{D}{d}\right)A_r + 0.491\,\mathrm{Re}_L^{0.532}\left(\frac{D}{L}\right)(1 - A_r) \tag{96}$$

Here, the area ratio is

$$A_r = \frac{d^2}{D^2}, \tag{97}$$

the approximate length of the wall jet region is $L = 0.5(D - d)$, d is the diameter of the jet just prior to impact, and both Reynolds numbers are based on the jet velocity just prior to impact. The correlation is derived from data for weakly turbulent jets impacting a nearly isothermal surface at $1250 < \mathrm{Re}_d \le 51000$ for $2.3 \le D/d \le 9.2$ and Pr = 7 or 25. It fits that data to ±15. The comparison to other existing data is also good, although the high Pr data of Metzger et al. are on average 20% below this correlation.

7.2 Moving Walls, Quenching, and Unsteadiness

Jet impingement onto moving surfaces is of importance in materials processing applications. For example, water jets are sometimes situated at the end of hot-rolling lines to quench the steel billets as they pass. Studies of jet impingement in these situations, and for other unsteady conditions, have been made by Zumbrunnen and co-workers [30,100–103] for planar jets and by Chen and Kothari [104] for circular jets. The use of planar jets for quenching processes has been surveyed by Viskanta and Incropera [105].

7.3 Applications to Electronics Cooling

A number of papers have investigated the potential use of impinging liquid jets for cooling high power-density electronics. The technical problem is to remove fairly large heat fluxes (typically from 10 to 200 W/cm^2) while maintaining relatively low temperature differences (semiconductor junction temperatures to be held below 85 or 100°C). Jets are attractive because of the high local heat transfer coefficient that can be achieved in the stagnation zone, which may be located atop an integrated circuit. A principal limitation that occurs is the need for dielectric coolants, such as FC-77, which cannot really match the thermal performance of water.

Typical designs may involve closely confined jets that are more nearly submerged than unsubmerged. Several designs have used arrays of jets for large area cooling, although difficulties arise in manifolding and exhausting the spent coolant. In addition, to circumvent the somewhat low h values achieved with fluorocarbon liquids, combinations of jets and finned surfaces have been tested, and designs that boil the coolant have been proposed. The interested reader is referred to the literature [81,106–110].

7.4 Boiling in Axisymmetric Jet Impingement

Nucleate boiling raises the impingement heat transfer coefficient markedly, at least in certain configurations [111]. The liquid may boil when the wall temperature exceeds the saturation temperature at the local pressure. The elevated liquid pressure at the stagnation point tends to suppress phase change there, but pressure returns to ambient pressure by a radius of about one jet diameter from the stagnation point. Thus, boiling typically begins at the outermost radius of the cooled surface where the liquid pressures are low and the wall temperatures are generally highest. Critical heat flux and burnout usually occur when boiling dries up the outflowing liquid sheet at the outer radius of the cooled target.

If heating is instead confined to the stagnation region, high pressure is maintained over the entire hot portion of the target, and the wall temperature required for nucleation is greater. The stagnation pressure can reach tens of atmospheres for jet velocities above 50 m/s; at such speeds, the already large h of the stagnation zone is augmented by a higher saturation temperature and a potentially very large difference between T_w and T_f, which can lead to enormous heat fluxes. At present, less is known about boiling and CHF processes in this configuration, even though it may be ideal for hot spot cooling. Estimated heat transfer coefficients for this configuration [112,113] have exceeded 1 MW/m^{2}K, with liquid-side temperature differences reaching several hundred kelvin.

7.4.1 Jet CHF for Large Area Targets. The available critical heat flux (CHF) data for jet impingement relate to fairly large ratios of cooled target diameter to jet

diameter. These studies were conducted by Katto, Monde, and co-workers [114-116] using jets of freon or water impinging on targets of 5 to 60 jet diameters in diameter. Nucleation was observed over a large radial band of the heater covering most of its surface downstream of the stagnation zone. Nucleation was not reported in the stagnation zone itself, although it was described as being within a diameter of it. CHF generally began at the outer edge of the heated disk and was often accompanied by dryout. Area-average critical heat fluxes of up to 18 MW/m^2 were reported.

Models and correlations have been developed for CHF in the jet/disk configuration [117]. These models show that vapor efflux and droplet ejection are critical to burnout. The ejection of droplets by vapor bubbles increases substantially with increasing heat flux and limits the supply of liquid to larger radii. In addition, kinematic splattering, as described in Section 6.1 for isothermal systems, will probably reduce the CHF on large area targets when the jet velocity is high or the jet length is long.

Arrays of jets have been implemented as a method of cooling still larger areas. This configuration has been studied by Monde and Inoue [18], who found that array CHF behavior was actually quite similar to single jet CHF. In particular, the single jet correlation of Sharan and Lienhard [117] accurately predicts the area-average CHF of jet arrays having as many as four jets.

7.4.2 Jet CHF for Stagnation Zone Heating. Very little data are available for boiling situations in which heating is confined to the stagnation region. The small areas here experience better liquid supply and higher pressures than in large-area CHF studies, and the dryout phenomena that occur in large-target cooling are no longer an issue. Nucleation behavior in this case, however, remains sketchy, and two questions appear to be central to understanding stagnation-zone CHF: how the very high local liquid pressure will affect the critical heat flux, and how boiling and CHF phenomena occur when heating is limited to a small area.

At high velocities, the stagnation-point pressure can become a significant fraction of the liquid's critical pressure, p_c Thermodynamic effects should be significant, in the sense of an increased saturation temperature and strongly altered physical properties and nucleation dynamics. Past work in various other boiling configurations has established that increasing pressure raises both the nucleate boiling heat flux (at a given wall superheat) and the critical heat flux. Maximum CHF occurs for pressures in the vicinity of 0.35 p_c, with rapidly decreasing CHF for pressures beyond 0.4 p_c. For water, this maximum CHF corresponds to pressures of about 70 atm in both pool and convective boiling [118]. For an impinging water jet, a stagnation-point pressure of 70 atm occurs at a jet speed of about 120 m/s. It seems reasonable to expect that heat flux (boiling and critical heat flux, as well as convective flux) will increase as jet speed is increased toward this value. Indeed, Liu and Lienhard [112] observed a monotonic increase in stagnation-point heat flux (at fixed wall superheat) as jet velocities were increased from 50 to 134 m/s.

A few studies have also examined boiling behavior for small heater sizes. Ma and Bergles [111] provide measurements of nucleate boiling heat fluxes during jet impingement of R-113 on a square heated region with a dimension of 2 to 3 jet

diameters. While they reported a trend toward a velocity-independent fully developed boiling curve as the flux increased, the velocities involved (10 m/s or less) were too low to cause a thermodynamically significant increase in the stagnation-point pressure. They did not provide direct data for CHF. Samant and Simon [119] examined boiling behavior from a small heated patch cooled by a parallel turbulent channel flow of FC-72. They saw no evidence of a burnout phenomenon at CHF; instead, the heat flux simply increased more slowly with increasing wall superheat in the transition and film boiling regions than in the nucleate regime.

Boiling in planar jet impingement has also been studied [120] and is surveyed by Viskanta and Incropera [105].

7.5 Extremely High Heat Fluxes in Jet Impingement

The highest heat fluxes obtained have generally been CHF values for tube flows of water, with maximum critical fluxes in the range of 100 to 350 MW/m^2. Usually, these critical fluxes are reached under large subcooling of the bulk liquid [121,122] by making the tube diameter small (a millimeter or two) and increasing the flow velocity to as much as 50 m/s. Even at these extreme conditions, the region over which high heat flux occurs is limited to a few centimeters along the length of the tube.

Liu and Lienhard [112,113] made a direct attempt to create extremely high heat fluxes using high velocity water jets to cool a small heated region. They confined the heating to the high-pressure stagnation region of a 1.9 mm diameter jet, so as to capitalize on the thermodynamic suppression phase change. Jet velocities ranged from 50 to 134 m/s, and associated stagnation pressures were between 12 and 89 atm. Their heat fluxes ranged between 50 and 400 MW/m^2 and include the highest steady state fluxes ever reported for any configuration.

Those experiments used thin metal targets heated on one side by a plasma arc and cooled on the opposite side by the jet. The arc side of the target was partially melted; temperatures through the target varied from the melting point temperature to a value of 100 to 300°C on the liquid side. In this condition, the targets were less than a millimeter in thickness.

After impact, the jets splattered much liquid, which prevented direct visualization of the stagnation zone. Thus, it was not possible to verify the presence or absence of phase change. However, Liu and Lienhard saw no evidence of a CHF or burnout phenomenon during stagnation-point heating. Their heat fluxes were generally limited by either the thermal power available for heating or by a mechanical failure of the targets (rupture in the form of fracture or plastic yielding). Failure depended on the target material used but not necessarily on its thermal conductivity. The highest fluxes were achieved using molybdenum targets; targets of steel, tungsten, and tantalum all failed at lower heat fluxes. The absence of a burnout process and the material dependence of target failure imply that liquid-side processes are not the principal factor limiting heat removal in these conditions.

From an engineering viewpoint, the limitations on stagnation-zone heat flux by jet impingement are associated with the structural integrity of the solid target rather than

the heat transfer coefficient. Temperatures and temperature gradients in the targets are very high; thermal stresses are large; and the extremely high flux experiments to date show that mechanical failure of the target tends to limit the achievable heat flux. To obtain still higher fluxes, better target materials are needed. As described by Lienhard and Khounsary [123], synthetic diamond films are an especially promising material for these high heat flux applications, owing to the high thermal conductivity of diamond and its low thermal expansion coefficient and high strength; and polycrystalline synthetic diamonds of relatively large size can now be produced by chemical vapor deposition processes.

REFERENCES

1. H. Rouse, J. W. Howe, and D. E. Metzler, Experimental Investigation of Fire Monitors and Nozzles, *Proc. ASCE Hyd. Div.*, Vol. 77, pp. 1–29, 1951.
2. M. Murakami and K. Katayama, Discharge Coefficients of Fire Nozzles, *J. Basic Eng.*, pp. 706–716, 1966.
3. S. J. Leach and G. L. Walker, The Application of High Speed Liquid Jets Cutting, *Phil. Trans. R. Soc. London A*, Vol. 260, pp. 295–308, 1966.
4. M. J. McCarthy and N. A. Molloy, Review of Stability of Liquid Jets and the Influence of Nozzle Design, *Chem. Eng. J.*, Vol. 7, pp. 1–20, 1974.
5. J. W. Hoyt and J. J. Taylor, Effect of Nozzle Boundary Layer on Water Jets Discharging in Air, in *Jets and Cavities — International Symposium*, ASME Winter Annual Meeting, FED-Vol. 31, pp. 93–100, 1985.
6. G. Birkhoff and E. H. Zarantonello, *Jets, Wakes, and Cavities*, Academic Press, New York, pp. 32-37; pp. 229-231, 1957.
7. J. H. Lienhard V and J. H. Lienhard, Velocity Coefficients for Free Jets from Sharp-Edged Orifices, *J. Fluids Engr.*, Vol. 106, pp. 13–17, 1984.
8. T. Morel, Comprehensive Design of Axisymnietric Wind Tunnel Contractions, *J. Fluids Eng.*, Vol. 97, pp. 225–233, 1975.
9. X. Liu, L. A. Gabour, and J. H. Lienhard V, Stagnation-Point Heat Transfer during Impingement of Laminar Liquid Jets: Analysis Including Surface Tension, *J. Heat Transfer*, Vol. 115, pp. 99–105, 1993.
10. J. H. Lienhard and J. B. Day, The Breaking of Superheated Liquid Jets, *J. Basic Eng.*, pp. 515–521, 1970.
11. J. T. Davies and R. W. Makepeace, Measurement of the Surface Ages of Water Jets, *AIChE J.*, Vol. 24, pp. 524–530, 1978.
12. J. L. Duda and J. S. Vrentas, Fluid Mechanics in Laminar Liquid Jets, *Chem. Eng. Sci.*, Vol. 22, p. 866, 1967.
13. J. Stevens and B. W. Webb, Measurements of the Free Surface Flow Structure Under an Impinging Free Liquid Jet, *J. Heat Transfer*, Vol. 114, pp. 79–84, 1992.
14. H. Martin, Heat and Mass Transfer between Impinging Gas Jets and Solid Surfaces, in *Advances in Heat Transfer*, Vol. 13, Academic Press, New York, 1977.
15. N. T. Obot, A. S. Mujumdar, and W. J. M. Douglas, Design Correlations for Heat and Mass Transfer under Various Turbulent Impinging Jet Configurations, in *Drying '80*, Hemisphere Publishing, New York, Vol. 1, pp. 388–402, 1980.
16. D. L. Besserman, F. P. Incropera, and S. Ramadhyani, Heat Transfer from a Square Source to an Impinging Liquid Jet Confined by an Annular Wall, *J. Heat Transfer*, Vol. 114, pp. 284–287, 1992.

17. S. Ishigai, S. Nakanishi, M. Mizuno, and T. Imamura, Heat Transfer of the Impinging Round Water Jet in the Interference Zone of Film Flow Along the Wall, *Bull. JSME*, Vol. 20, pp. 85–92, 1977.
18. M. Monde and T. Inoue, Critical Heat Flux in Saturated Forced Convective Boiling on a Heated Disk with Multiple Impinging Jets, *J. Heat Transfer*, Vol. 113, pp. 722–727, 1991.
19. J. Kevorkian and J. D. Cole, *Perturbation Methods in Applied Mathematics*, Springer-Verlag, New York, Section 4.2, pp. 370-387, 1981.
20. K. Hiemenz, Die Grenzschicht an einem in den gleichformigen Flussigkeitsstrom eingetauchten geraden Kreiszylinder, *Dingler's Polytech. J.*, Vol. 326, p. 321, 1911.
21. F. Homann, Der Einfluss grosser Zahigkeit bei der Strommung um den Zylinder und um die Kugel, *Z. Angew. Math. Mech.*, Vol. 16, pp. 153–164, 1936.
22. L. Howarth, The Boundary Layer in Three-Dimensional Flow—Part II. The Flow Near a Stagnation Point, *Phil. Mag.*, Series. 7, Vol. 42, pp. 1433–1440, 1951.
23. G. K. Batchelor, *An Introduction to Fluid Dynamics*, Cambridge University Press, Cambridge, Great Britain, p. 105, 1967.
24. W. Schach, Umlenkung eines freien Flussigkeitsstrahles an einer ebenen Platte, *Ing.-Arch*, Vol. 5, pp. 245–265, 1934.
25. W. Schach, Umlenkung eines kreisformigen Flussigkeitsstrahles an einer ebenen Platte senkrecht zur Stromungsrichtung, *Ing.-Arch*, Vol. 6, pp. 51–59, 1935.
26. Y. C. Shen, Theoretical Analysis of Jet-Ground Plane Interaction, *IAS Paper No. 62–144*, 1962.
27. T. Strand, On the Theory of Normal Ground Impingement of Axisymmetric Jets in Inviscid Incompressible Flow, *AIAA Paper No. 64–424*, 1964.
28. M. T. Scholtz and O. Trass, Mass Transfer in a Nonuniform Impinging Jet, *AIChE J.*, Vol. 16, pp. 82–96, 1970.
29. L. M. Milne-Thomson, *Theoretical Hydrodynamics*, 4th ed., Chap. 11, Sec. 11.41, MacMillan, New York, 1960.
30. D. A. Zumbrunnen, F. P. Incropera, and R. Viskanta, Convective Heat Transfer Distributions on a Plate Cooled by Planar Water Jets, *J. Heat Transfer*, Vol. 111, pp. 889–895, 1989.
31. S. Inada, Y. Miyasaka, and R. Izumi, A Study on the Laminar-flow Heat Transfer between a Two-dimensional Water Jet and a Flat Surface with Constant Heat Flux, *Bull. JSME*, Vol. 24, pp. 1803–1810, 1981.
32. T. Strand, Inviscid-Incompressible-Flow Theory of Static Two-Dimensional Solid Jets in Proximity to the Ground, *J. Aerospace Sci.*, Vol. 29, p. 170, 1962.
33. H. Miyazaki and E. Silberman, Flow and Heat Transfer on a Flat Plate Normal to a Two-Dimensional Laminar Jet Issuing From a Nozzle of Finite Height, *Int. J. Heat Mass Transfer*, Vol. 25, pp. 2097–2107, 1972.
34. E. M. Sparrow and L. Lee, Analysis of Flow Field and Impingement Heat/Mass Transfer Due to a Nonuniform Slot Jet, *J. Heat Transfer*, Vol. 97, pp. 191–197, 1975.
35. D. H. Wolf, R. Viskanta, and F. P. Incropera, Local Convective Heat Transfer from a Heated Surface to a Planar Jet of Water with a Nonuniform Velocity Profile, *J. Heat Transfer*, Vol. 112, pp. 899–905, 1990.
36. S. Goldstein, *Modern Developments in Fluid Dynamics*, Oxford University Press, London, 1938.
37. M. Sibulkin, Heat Transfer Near the Forward Stagnation Point of a Body of Revolution, *J. Aeronaut. Sci.*, Vol. 19, pp. 570–571, 1952.
38. V. M. Falkner and S. W. Skan, *Some Approximate Solutions of the Boundary Layer Equations*, ARC R&M, No. 1314, 1930.
39. A. Fage and V. M. Falkner, *Relation between Heat Transfer and Surface Friction for Laminar Flow*, ARC R&M, No. 1408, 1931.

40. W. Mangler, *Ber. Aerodyn. Versuchsanst. Goett. Rep.*, 45/A/17, 1945, *Z. Angew. Math. Mech.*, Vol. 28, pp. 97-103, 1948.
41. F. M. White, *Viscous Fluid Flow*, McGraw-Hill, New York, pp. 172–184, 1974.
42. C. W. Jones and E. J. Watson, Two-Dimensional Boundary Layers, Chap. 5 in L. Rosenhead, *Laminar Boundary Layers*, Oxford University Press, Great Britain, p. 198, 1963.
43. X. S. Wang, Z. Dagan, and L. M. Jiji, Heat Transfer between A Circular Free Impinging Jet and a Solid Surface with Non-uniform Wall Temperature or Wall Heat Flux — 1. Solution for the Stagnation Region, *Int. J. Heat Mass Transfer*, Vol. 32, pp. 1351–1360, 1989.
44. X. Liu, J. H. Lienhard V, and J. S. Lombara, Convective Heat Transfer by Impingement of Circular Liquid Jets, *J. Heat Transfer*, Vol. 113, pp. 571–582, 1991.
45. V. E. Nakaryakov, B. G. Pokusaev, and E. N. Troyan, Impingement of an Axisymmetric Liquid Jet on a Barrier, *Int. J. Heat Mass Transfer*, Vol. 21, pp. 1175–1184, 1978.
46. A. M. Khounsary, personal communications, Jan.-July, 1993.
47. A. M. Khounsary, J. J. Chrzas, D. M. Mills, and P. J. Viccaro, Performance Analysis of High-Power Synchrontron X-ray Monochromators, *Optical Eng.*, Vol. 29, pp. 1273–1280, 1990.
48. E. M. Sparrow and T. C. Wong, Impingement Transfer Coefficients Due to Initially Laminar Slot Jets, *Int. J. Heat Mass Trans.*, Vol. 18, pp. 597–605, 1975.
49. V. K. Garg and S. Jayaraj, Boundary Layer Analysis for Two-Dimensional Slot Jet Impingement on Inclined Plates, *J. Heat Transfer*, Vol. 110, pp. 577–582, 1988.
50. J. Stevens, Y. Pan, and B. W. Webb, Effect of Nozzle Configuration on Transport in the Stagnation Zone of Axisymmetric Impinging Free-Surface Liquid Jets: Part 1 — Turbulent Flow Structure, *J. Heat Transfer*, Vol. 114, pp. 874–879, 1992.
51. J. W. Stevens, Measurements of Local Fluid Velocities in an Axisymmetric Free Liquid Jet Impinging on a Flat Plate, Ph.D. thesis, Brigham Young University, Provo, Utah, 1991.
52. S. Sikmanovic, S. Oka, and S. Koncar-Djurdjevic, Influence of the Structure of Turbulent Flow on Heat Transfer from a Single Cylinder in a Cross Flow, *Proc. 5th Int. Heat Trans. Conf.*, Tokyo, Vol. 2, pp. 320–324, 1974.
53. G. W. Lowery and R. I. Vachon, The Effect of Turbulence on Heat Transfer from Heated Cylinders, *Int. J. Heat Mass Trans.*, Vol. 18, pp. 1229–1242, 1975.
54. A. B. Mehendale, J. C. Han, and S. Ou, Influence of High Mainstream Turbulence on Leading Edge Heat Transfer, *J. Heat Transfer*, Vol. 113, pp. 843–850, 1991.
55. R. Gardon and J. C. Akfirat, The Role of Turbulence in Determining the Heat Transfer Characteristics of Impinging Jets, *Int. J. Heat Mass Trans.*, Vol. 8, pp. 1261–1272, 1965.
56. S. G. Simmons, J. M. Hager, and T. E. Diller, Simultaneous Measurements of Time-Resolved Surface Heat Flux and Freestream Turbulence at a Stagnation Point, *Heat Transfer 1990*, Hemisphere Publishing, Bristol, PA, Vol. 2, pp. 375–380, 1990.
57. D. T. Vader, F. P. Incropera, and R. Viskanta, Local Convective Heat Transfer from a Heated Surface to an Impinging Planar Jet of Water, *Int. J. Heat Mass Trans.*, Vol. 34, pp. 611–623, 1991.
58. Y. Pan, J. Stevens, and B. W. Webb, Effect of Nozzle Configuration on Transport in the Stagnation Zone of Axisymmetric Impinging Free-Surface Liquid Jets. Part 2. Local Heat Transfer, *J. Heat Transfer*, Vol. 114, pp. 880–886, 1992.
59. S. Faggiani and W. Grassi, Round Liquid Jet Impingement Heat Transfer: Local Nusselt Numbers in the Region with Non Zero Pressure Gradient, *Proc. of the Ninth Int. Heat Trans. Conf.*, Vol. 4, pp. 197–202, 1990.
60. L. A. Gabour and J. H. Lienhard V, Wall Roughness Effects on Stagnation Point Heat Transfer Beneath an Impinging Liquid Jet, *29th ASME/AIChE Natl. Heat Trans. Conf.*, Atlanta, Aug. 8–11; *J. Heat Transfer*, Vol. 116, pp. 81–87, 1994.

61. J. Stevens and B. W. Webb, Local Heat Transfer Coefficients Under an Axisymmetric Single-Phase Liquid Jet, *J. Heat Transfer*, Vol. 113, pp. 71–78, 1991.
62. X. S. Wang, Z. Dagan, and L. M. Jiji, Conjugate Heat Transfer between a Laminar Impinging Liquid Jet and a Solid Disk, *Int. J. Heat Mass Transfer*, Vol. 32, pp. 2189–2197, 1989.
63. X. S. Wang, Z. Dagan, and L. M. Jiji, Heat Transfer between a Laminar Free-Surface Impinging Jet and a Composite Disk, *Proc. Ninth Int. Heat Transfer Conf.*, Vol. 4, p. 137, 1990.
64. D. T. Vader, F. P. Incropera, and R. Viskanta, A Method for Measuring Steady Local Heat Transfer to an Impinging Liquid Jet, *Exp. Thermal Fluid Sci.*, Vol. 4, pp. 1–11, 1991.
65. C. B. Reed, Convective Heat Transfer in Liquid Metals, in *Handbook of Single-Phase Convective Heat Transfer*, Chap. 8, (eds. S. Kakac, R. K. Shah, and W. Aung), John Wiley & Sons, New York, 1987.
66. P. F. Sullivan, S. Ramadhyani, and F. P. Incropera, Use of Smooth and Roughened Spreader Plates to Enhance Impingement Cooling of Small Heat Sources with Single Circular Liquid Jets, *28th ASME/AIChE National Heat Transfer Conf.*, San Diego, CA, 1992.
67. J. Stevens and B. W. Webb, The Effect of Inclination on Local Heat Transfer under an Axisymmetric Free Liquid Jet, *Int. J. Heat Mass Trans.*, Vol. 34, pp. 1227–1236, 1991.
68. D. C. McMurray, P. S. Myers, and 0. A. Uyehara, Influence of Impinging Jet Variables on Local Flat Surface with Constant Heat Flux, *Proc. 3rd Int. Heat Trans. Conf.*, pp. 292–299, 1966.
69. E. J. Watson, The Radial Spread of a Liquid Jet over a Horizontal Plane, *J. Fluid Mech.*, Vol. 20, pp. 481–499, 1964.
70. X. Liu and J. H. Lienhard V, The Hydraulic Jump in Circular Jet Impingement and in Other Thin Liquid Films, *Exp. Fluids*, Vol. 15, pp. 108–116, 1993.
71. T. Azuma and T. Hoshino, LDV Measurement in Radial Flow of Thin Liquid Film, *Proc. of the Osaka Symposium on Flow Measuring Techniques*, pp. 1–15, 1983.
72. T. Azuma and T. Hoshino, The Radial Flow of a Thin Liquid Film (1st Report, Laminar Turbulent Transition), *Bull. JSME*, Vol. 27, pp. 2739–2746, 1984.
73. T. Azuma and T. Hoshino, The Radial Flow of a Thin Liquid Film (2nd Report, Liquid Film Thickness), *Bull. JSME*, Vol. 27, pp. 2747–2754, 1984.
74. T. Azuma and T. Hoshino, The Radial Flow of A Thin Liquid Film (3rd Report, Velocity Profile), *Bull. JSME*, Vol. 27, pp. 2755–2762, 1984.
75. T. Azuma and T. Hoshino, The Radial Flow of a Thin Liquid Film (4th Report, Stability of Liquid Film and Wall Pressure Fluctuation), *Bull JSME*, Vol. 27, pp. 2763–2770, 1984.
76. R. G. Olsson and E. T. Turkdogan, Radial Spread of a Liquid Stream on a Horizontal Plate, *Nature*, Vol. 211, pp. 813–816, 1966.
77. A. Sharan, Jet-disc Boiling: Bumout Predictions and Application to Solar Receivers, Master's thesis, University of Houston, Houston, TX, 1984.
78. X. S. Wang, Z. Dagan, and L. M. Jiji, Heat Transfer between a Circular Free Impinging Jet and a Solid Surface with Non-uniform Wall Temperature or Wall Heat Flux. II. Solution for the Boundary Layer Region, *Int. J. Heat Mass Trans.*, Vol. 32, pp. 1361–1371, 1989.
79. X. Liu and J. H. Lienhard V, Liquid Jet Impingement Heat Transfer on a Uniform Flux Surface, *Heat Transfer Phenomena in Radiation, Combustion, and Fires*, ASME, HTD, Vol.106, pp. 523–530, 1989.
80. Z. H. Chaudhury, Heat Transfer in a Radial Liquid Jet, *J. Fluid Mech.*, Vol. 20, pp. 501–511, 1964.
81. D. J. Womac, S. Ramadhyani, and F. P. Incropera, Correlating Equations for Impingement Cooling of Small Heat Sources with Single Circular Liquid Jets, *J. Heat Transfer*, Vol. 115, pp. 106–115, 1993.

82. A. J. Peterka, Hydraulic Design of Stilling Basins and Energy Dissipators. U. S. Dept. Interior, Bur. Reclamation, Eng. Monograph 25, 1963.
83. M. Bouhadef, Etalement en couche mince d'un jet liquids cylinchique vertical sur un plan horizontal, *J. de Mathematiques et de Physique Appliquees,* Vol. 29, pp. 157–167, 1978.
84. A. D. D. Craik, R. C. Latham, M. J. Fawkes, and P. W. F. Gribbon, The Circular Hydraulic Jump, *J. Fluid Mech.,* Vol. 112, pp. 347–362, 1981.
85. M. Errico, A Study of the Interaction of Liquid Jets with Solid Surfaces, Ph. D. Dissertation, University of California at San Diego, San Diego, CA, 1986.
86. V. K. Vasista, Experimental Study of the Hydrodynamics of an Impinging Liquid Jet, S. B. Thesis, Massachusetts Institute of Technology, Cambridge, MA, 1989.
87. S. Thomas, A. Faghri, and W. Hankey, Experimental Analysis and Flow Visualization of a Thin Liquid Film on a Stationary and Rotating Disk, *J. Fluids Eng.,* Vol. 113, pp. 73–80, 1991.
88. M. M. Rahman, A. Faghri, W. L. Hankey, and T. D. Swanson, Prediction of Heat Transfer to a Thin Liquid Film in Plane and Radially Spreading Flows, *J. Heat Transfer,* Vol. 112, pp. 822–825, 1990.
89. M. M. Rahman, A. Faghri, and W. L. Hankey, Computation of Turbulent Flow in a Thin Liquid Layer of Fluid Involving a Hydraulic Jump, *J. Fluids Eng.,* Vol. 113, pp. 411–413, 1991.
90. S. Thomas, W. Hankey, A. Faghri, and T. Swanson, One-Dimensional Analysis of the Hydrodynamic and Thermal Characteristics of Thin Film Flows Including the Hydraulic Jump and Rotation, *J. Heat Transfer,* Vol. 112, pp. 728–735, 1990.
91. J. H. Lienhard V, X. Liu, and L. A. Gabour, Splattering and Heat Transfer During Impingement of a Turbulent Liquid Jet, *J. Heat Transfer,* Vol. 114, pp. 362–372, 1992.
92. D. A. Varela and J. H. Lienhard V, Development of Non-linear Waves on a Nonuniform Axisymmetric Film, *Bull. Am. Phy. Soc.,* A18, Vol. 36, pp. 2625; *44th Annu. Meet. Div. Fluid Dynamics,* Scottsdale, 1991.
93. D. A. Varela Cristales, Nonlinear Waves on the Surface of A Radially Flowing Film, M.S. Thesis, Massachusetts Institute of Technology, Cambridge, MA, 1992.
94. P. G. Drazin and W. H. Reid, *Hydrodynamic Stability,* Cambridge University Press, London, England, pp. 22–27, 1981.
95. S. K. Bhunia and J. H. Lienhard V, Splattering during Turbulent Liquid Jet Impingement on Solid Targets, *J. Fluids Eng.,* Vol. 116, pp. 338–344, 1994.
96. S. K. Bhunia and J. H. Lienhard V, Surface Disturbance Evolution and the Splattering of Turbulent Liquid Jets, *J. Fluids Eng.,* Vol. 116, pp. 721–727, 1994.
97. W. K. George, P. D. Beuther, and R. E. A. Arndt, Pressure Spectra in Turbulent Free Shear Flows, *J. Fluid Mech.,* Vol. 148, pp. 155–191, 1984.
98. D. E. Metzger, K. N. Cummings, and W. A. Ruby, Effects of Prandtl Number on Heat Transfer Characteristics of Impinging Liquid Jets, *Proc. of Fifth Int. Heat Transfer Conf.,* Vol. II, pp. 20–24, 1974.
99. D. J. Womac, G. Aharoni, S. Ramadhyani, and F. P. Incropera, Single Phase Liquid Jet Impingement Cooling of Small Heat Sources, *Proc. Ninth Int. Heat Transfer Conf.,* Vol. 4, pp. 149–154, 1990.
100. D. A. Zumbrunnen, Convective Heat and Mass Transfer in the Stagnation Region of a Planar Jet Impinging on a Moving Surface, *J. Heat Transfer,* Vol. 113, pp. 563–570, 1991.
101. D. A. Zumbrunnen, Transient Convective Heat Transfer in Planar Stagnation Flows With Time-Varying Surface Heat Flux and Temperature, *J. Heat Transfer,* Vol. 114, pp. 85–93, 1992.
102. D. A. Zumbrunnen and M. Azia, Convective Heat Transfer Enhancement Due to Intermittency in an Impinging Jet, *Proc. 28th Natl. Heat Transfer Conf. and Exhibition,* HTD, Vol. 202, pp. 39–47, 1992.

103. D. A. Zumbrunnen, F. P. Incropera, and R. Viskanta, A Laminar Boundary Layer Model of Heat Transfer Due to a Nonuniform Planar Jet Impinging on a Moving Plate, *Warme-und Stoffubertragung,* Vol. 27, pp. 311–319, 1992.
104. S. J. Chen and J. Kothari, Temperature Distribution and Heat Transfer of a Moving Metal Strip Cooled by a Water Jet, ASME Paper 88-WA/NE-4, WAM, Chicago, IL, 1988.
105. R. Viskanta and F. P. Incropera, Quenching with Liquid Jet Impingement, in *Heat and Mass Transfer in Material Processing,* (eds. I. Tanasawa and N. Lior), Hemisphere Publishing, New York, pp. 455–476, 1992.
106. C. F. Ma and A. E. Bergles, Boiling Jet Impingement Cooling of Simulated Microelectronic Chips, *Heat Transfer in Electronic Equipment — 1983,* HTD, Vol. 28, pp. 5–12, ASME, New York, 1983.
107. L. M. Jiji and Z. Dagan, Experimental Investigation of Single-Phase Multijet Impingement Cooling of an Array of Microelectronic Heat Sources, (ed. W. Aung), in *Cooling Technology for Electronic Equipment,* Hemisphere Publishing, New York, pp. 333–351, 1988.
108. D. C. Wadsworth and I. Mudawar, Cooling of a Multichip Electronic Module by Means of Confined Two-Dimensional Jets of Dielectric Liquid, *J. Heat Transfer,* Vol. 112, pp. 891–898, 1990.
109. I. Mudawar and D. C. Wadsworth, Critical Heat Flux from a Simulated Chip to a Confined Rectangular Impinging Jet of Dielectric Liquid, *Int. J. Heat Mass Trans.,* Vol. 34, pp. 1465–1479, 1991.
110. D. C. Wadsworth and I. Mudawar, Enhancement of Single-Phase Heat Transfer and Critical Heat Flux From an Ultra-High-Flux Simulated Microelectronic Heat Source to a Rectangular Impinging Jet of Dielectric Liquid, *J. Heat Transfer,* Vol. 114, pp. 764–768, 1992.
111. C. F. Ma and A. E. Bergles, Jet Impingement Nucleate Boiling, *Int. J. Heat Mass Trans.,* Vol. 29, pp. 1095–1101, 1986.
112. X. Liu and J. H. Lienhard V, Extremely High Heat Fluxes Beneath Impinging Liquid Jets, *J. Heat Transfer,* Vol. 115, pp. 472–476, 1993.
113. X. Liu and John H. Lienhard V, Extremely High Heat Flux Removal by Subcooled Liquid Jet Impingement, in *Fundamentals of Subcooled Flow Boiling,* ASME, HTD, Vol. 217, pp. 11–20, 1992.
114. Y. Katto and M. Shimizu, Upper Limit of CHF in the Saturated Forced Convection Boiling on a Heated Disk with a Small Impinging Jet, *J. Heat Transfer,* Vol. 101, pp. 265–269, 1979.
115. M. Monde and Y. Katto, Burnout in a High Heat-Flux Boiling System with an Impinging Jet, *Int. J. Heat Mass Trans.,* Vol. 21, pp. 295–305, 1978.
116. M. Monde, Critical Heat Flux in Saturated Forced Convection Boiling on a Heated Disk with an Impinging Jet, *J. Heat Transfer,* Vol. 109, pp. 991–996, 1987.
117. A. Sharan and J. H. Lienhard, On Predicting Burnout in the Jet-Disk Configuration, *J. Heat Transfer,* Vol. 107, pp. 398–401, 1985.
118. P. B. Whalley, *Boiling, Condensation and Gas-Liquid Flow,* Oxford University Press, New York, 1987.
119. K. R. Samant and T. W. Simon, Heat Transfer Form a Small Heated Region to R-113 and FC-72, *J. Heat Transfer,* Vol. 111, pp. 1053–1059, 1989.
120. D. T. Vader, F. P. Incropera, and R. Viskanta, Convective Nucleate Boiling on a Heated Surface Cooled by an Impinging Planar Jet of Water, *J. Heat Transfer,* Vol. 114, pp. 152–160, 1992.
121. R. D. Boyd, Subcooled Flow Boiling Critical Heat Flux (CHF) and Its Application to Fusion Energy Components. Part II. A Review of Microconvective, Experimental, and Correlational Aspects, *Fusion Technol.,* Vol. 7, pp. 3i–52, 1985.

122. G. R. Beitel, Boiling Heat-Transfer Processes and Their Application in the Cooling of High Heat Flux Devices, AEDC-TR-93-3, Arnold Air Force Base, Tennessee, June 1993.
123. J. H. Lienhard V and A. M. Khounsary, Liquid Jet Impingement Cooling with Diamond Substrates for Extremely High Heat Flux Applications, *High Heat Flux Engineering II,* SPIE Vol. 1997, pp. 29–43, 1993.

CORRECTIONS OF LAMINAR IMPINGING JET EQUATIONS

J.H. LIENHARD V

The equation for C_3 is a bit complicated, and it has repeatedly carried typographical errors of one sort or another. These errors appear in: Liu and Lienhard (1989, eq. 16); Liu, Lienhard and Lombara (1991, eq. 4); Lienhard (1995, Table 5); and Lienhard (2006, eq. 36).

The correct equation for C_3 is:

$$C_3 = \frac{0.267(d/r_0)^{1/2}}{\left[0.1713\,(d/r_0)^2 + (5.147\,r_0/\mathrm{Re}_d\,d)\right]^2\,\mathrm{Re}_d^{1/2}} - \frac{1}{2}\left(\frac{r_0}{d}\right)^2 \tag{1}$$

Equation (78) and Table 5 in Lienhard (1995) give an incorrect expression for Nu_d. The correct expression is:

$$\mathrm{Nu}_d = \frac{q_w\,d}{k(T_w - T_f)} = \frac{8\,\mathrm{Re}_d\mathrm{Pr}\,f(C_f,\mathrm{Pr})}{49\,(hr/d^2) + 28\,(r/d)^2\,f(C_f,\mathrm{Pr})} \tag{2}$$

References

[1] X. Liu and J.H. Lienhard V, 1989, "Liquid Jet Impingement Heat Transfer on Uniform Heat Flux Surface," *Heat Transfer Phenomena in Radiation, Combustion, and Fires*, ASME HTD, Vol.106, pp.523-530. (26th ASME/AIChE National Heat Transfer Conference, Philadelphia, Aug. 6-9, 1989)

[2] X. Liu, J.H. Lienhard V, and J.S. Lombara, 1991, "Convective Heat Transfer by Impingement of Circular Liquid Jets," *J. Heat Transfer,* Vol. 113, No. 3, pp. 571-582.

[3] J.H. Lienhard V, 1995, "Liquid Jet Impingement," *Annual Review of Heat Transfer,* C.L. Tien ed., Vol. 6, Chpt. 4. New York: Begell House, pp. 199-270.

[4] J.H. Lienhard V, 2006, "Heat Transfer by Impingement of Circular Free-surface Liquid Jets," in S.C. Mishra, B.V.S.S.S. Prasad, and S.V. Garimella (eds.), *Heat and Mass Transfer 2006*. New Delhi: Tata McGraw-Hill, pp. 211–226. (Proc. 18th Natl. and 7th Intl. ISHMT-ASME Heat and Mass Transfer Conf., Guwahati, India 4–6 Jan. 2006).

Date: July 6, 2015.